

THREE-DIMENSIONAL SIMULATIONS OF MAGNETIZED SUPERBUBBLES: NEW INSIGHTS INTO THE IMPORTANCE OF MHD EFFECTS ON OBSERVED QUANTITIES

JEROEN STIL, NICOLE WITYK, RACHID OUYED, AND A. R. TAYLOR

Department of Physics and Astronomy, University of Calgary, 2500 University Drive NW, Calgary, Alberta, T2N 1N4 Canada

Accepted for publication in The Astrophysical Journal

ABSTRACT

We present three-dimensional magnetohydrodynamic (MHD) simulations of superbubbles, to study the importance of MHD effects in the interpretation of images from recent surveys of the Galactic plane. These simulations focus mainly on atmospheres defined by an exponential density distribution and the Dickey & Lockman (1990) density distribution. In each case, the magnetic field is parallel to the Galactic plane and we investigate cases with either infinite scale height (constant magnetic field) or a constant ratio of gas pressure to magnetic pressure. The three-dimensional structure of superbubbles in these simulations is discussed with emphasis on the axial ratio of the cavity as a function of magnetic field strength and the age of the bubble. We investigate systematic errors in the age of the bubble and scale height of the surrounding medium that may be introduced by modeling the data with purely hydrodynamic models. Age estimates derived with symmetric hydrodynamic models fitted to an asymmetric magnetized superbubble can differ by up to a factor of four, depending on the direction of the line of sight. The scale height of the surrounding medium based on the Kompaneets model may be up to 50% lower than the actual scale height. We also present the first ever predictions of Faraday rotation by a magnetized superbubble based on three-dimensional MHD simulations. We emphasize the importance of MHD effects in the interpretation of observations of superbubbles.

Subject headings: ISM: bubbles, magnetic fields – methods: numerical – ISM: individual (W4)

1. INTRODUCTION

The combined stellar wind and supernova ejecta of groups of O and B stars blow large bubbles in the interstellar medium. The largest of these bubbles, with size scales of 100 pc to 1 kpc are commonly referred to as superbubbles. The basic structure of a superbubble consists of a hot low-density interior, the cavity, surrounded by a cool shell of swept-up interstellar medium. The continuous formation and dissipation of superbubbles is an important factor in the energy balance of the interstellar medium, and determines the locations of different phases of the interstellar medium on large scales (McKee & Ostriker 1977). Compression of the interstellar medium in the shell may increase cooling and trigger the formation of a new generation of stars. Also, the ability of large superbubbles to break out of the disk of a galaxy and initiate an outflow of chemically enriched plasma and ionizing radiation from the disk into the halo has a profound influence on the evolution of galaxies.

Several examples of well-defined superbubbles have been identified in the Galaxy (e.g. Heiles 1984; Maciejewski et al. 1996; Normandeau et al. 1996; Heiles 1998; Ehlerová & Palous 1999; Callaway et al. 2000; Reynolds et al. 2001; McClure-Griffiths et al. 2002; Pidopryhora et al. 2007). These have been studied in detail, thanks to their relative proximity. Observations with parsec-scale resolution of neutral and ionized gas reveal important details about the interaction between the hot ejecta and the interstellar medium. New high-resolution surveys of Galactic atomic hydrogen (HI) emission (Taylor et al. 2003; McClure-Griffiths et al. 2005; Stil et al. 2006) have provided unprecedented images with morphological and kinematic information of Galactic superbub-

bles (Normandeau et al. 1996; McClure-Griffiths et al. 2003). Physically interesting parameters are usually derived from the observations by means of analytic models that assume spherical symmetry (Castor et al. 1975; Weaver et al. 1977) or axial symmetry (Kompaneets 1960; Basu et al. 1999).

In this paper we investigate the importance of MHD effects on physical quantities derived from observed superbubbles. The effect of the Galactic magnetic field is difficult to model because it introduces anisotropy in the medium, which requires three-dimensional numerical simulations. The first three-dimensional magnetohydrodynamic simulations of superbubbles were presented by Tomisaka (1998), who discussed the importance of the magnetic field in the break-out of superbubbles from the Galactic disk. Tomisaka (1998) also described significant departures from spherical and axial symmetry in the shape of a magnetized bubble resulting from the interaction of the expanding superbubble with the Galactic magnetic field. The shape and the size of a superbubble depend on the strength and the geometry of the Galactic magnetic field as much as they depend on the density distribution of the ambient interstellar medium. The expanding superbubble in turn redefines the geometry of the interstellar medium and the Galactic magnetic field in a volume several hundred parsecs across.

Korpi et al. (1999) and de Avillez & Breitschwerdt (2005) performed three-dimensional MHD simulations that include the evolution of a superbubble in a supernova-driven turbulent multi-phase interstellar medium. The super bubbles in these simulations show significant departures from symmetry because of inhomogeneities in the medium in which the super bubble expands. Korpi et al. (1999) and de Avillez & Breitschwerdt (2005) found that a super

bubble can break out into the halo in such a medium. Although these simulations provide valuable insight in the dynamics of superbubbles in a multi-phase interstellar medium, it is in general difficult to relate these simulations to specific observed super bubbles (see however Fuchs et al. 2006 for a simulation of the Local Bubble).

Astrophysical parameters derived from observations, such as the age and the energy of a superbubble, or the density distribution of the ambient medium have relied on symmetric analytic models that do not include a magnetic field. The departure from axial symmetry imposed by the magnetic field introduces systematic errors that have not been considered before. In this paper we present three-dimensional MHD simulations of superbubbles, and we explore the errors introduced by commonly used methods to determine basic parameters from observations. In particular, we study the axial ratio of the wind-blown cavity for different times and magnetic field configurations. The smaller simulation volume and time span used in our simulations compared to Tomisaka (1998) are more tailored to the latitude coverage of the Galactic plane surveys. We also calculate the first images of Faraday rotation by a magnetized superbubble derived from our simulations, and emphasize the importance of such simulations to make meaningful predictions in this area.

We describe frequently used analytic models §2 and detail our numerical setup and methods in §3. Numerical results and the analysis of magnetic effects on derived parameters are presented §4. The specific case of the W4 superbubble is discussed in §5. Faraday rotation by magnetized superbubbles is discussed in §6, and conclusions are presented in §7.

2. ANALYTIC HYDRODYNAMIC MODELS OF BUBBLES

The exact shape and size of the bubble depends directly on the environment and the strength of the source. For weaker sources which produce bubbles whose extent are much smaller than the scale height of the gas in the galaxy, a solution with an approximately constant density profile may be considered. Castor et al. (1975) present a solution for a spherical wind-blown bubble expanding into a non-magnetized medium, in which the radius of the bubble varies according to

$$R_b(t) = 0.76 \left(\frac{L_s t^3}{\rho} \right)^{1/5} = 55.2 \left(\frac{L_s}{3 \times 10^{37} \text{ erg s}^{-1}} \right)^{1/5} \times \left(\frac{\rho}{1.67 \times 10^{-24} \text{ g cm}^{-3}} \right)^{-1/5} t_6^{3/5} \text{ pc.} \quad (1)$$

where R_b is the outer shock of the shell, L_s is the mechanical luminosity of the source, ρ is the ambient density of the undisturbed interstellar medium, and t_6 is the age of the bubble in Myr. The radius of the contact discontinuity was found to be $0.86R_b$ by Weaver et al. (1977).

For larger bubbles, associated with powerful sources, the situation is more complicated. The gravitational potential of the Galactic disk produces a density gradient perpendicular to the plane of the disk. At early stages, the Castor et al. (1975) solution can still be applied, but

as the radius of the bubble exceeds the scale height of the surrounding medium, the density gradient of the surrounding medium affects the shape of the bubble.

Kompaneets (1960) (hereafter K60) proposed a solution for the evolution of a point explosion in a non-magnetized exponential atmosphere that can be applied to this situation. This solution is based on the assumptions that the thermal energy is a constant fraction of the energy deposited in the initial blast and that the energy distribution is uniform throughout the volume of the bubble except close to the shock front where the energy density can be two to three times the mean value (see also Bisnovatyi-Kogan & Silich 1995). Basu et al. (1999) extended the Kompaneets solution to describe continuous energy injection, which we use in this paper. The source is located at $z = 0$ in an exponential atmosphere with scale height H of the form

$$\rho(z) = \rho_o e^{-z/H}. \quad (2)$$

The radius of the bubble in cylindrical coordinates takes the following form

$$R = 2H \arccos \left[\frac{1}{2} e^{z/2H} \left(1 - (\tilde{y}/2)^2 + e^{-z/H} \right) \right] \quad (3)$$

where

$$\tilde{y} = \frac{1}{H} \int_0^t \sqrt{\frac{\gamma^2 - 1}{2} \frac{E_{th}}{\rho_0 \Omega}} dt' \quad (4)$$

is a dimensionless transformed time variable, γ is the adiabatic index, E_{th} is the thermal energy of the bubble, and Ω is the volume of the bubble.

The independent variables are the mass density at $z = 0$ (ρ_0), the scale height of the atmosphere (H), and the mechanical luminosity of the source (L_s), which determines E_{th} . The unit of time in this model is then defined by

$$t_{0,k} = \left(\frac{\rho_0 H^5}{L_s} \right)^{1/3}. \quad (5)$$

For $R = 0$, Equation (3) reduces to two equations for the upper and lower boundary of the blast wave, z_1 and z_2 respectively (Basu et al. 1999)

$$z_{1,2} = -2H \ln \left(1 \mp \frac{\tilde{y}}{2} \right) \quad (6)$$

As \tilde{y} approaches 2, the top of the bubble in the Kompaneets model expands to infinite height in a finite amount of time. Physically, this means the shock acceleration in the z -direction becomes infinite because of the strong density gradient (Bisnovatyi-Kogan & Silich 1995). The bottom of the bubble (z_2 , Equation 6) does not penetrate downward more than $2H \ln 2 \approx 1.4H$, its location at the time of blow-out. Since the top of the Kompaneets model reaches an infinite height in a finite amount of time, it cannot be a valid solution at later times. However, it can provide an adequate solution at early times, if the initial conditions are consistent with the assumptions of the Kompaneets model, i.e. negligible pressure of the ambient medium and negligible inertia of the swept up medium.

With the addition of a magnetic field, no three-dimensional analytic solutions exist. In order to capture

the true evolution of these bubbles numerical simulations need to be performed.

3. SIMULATION SETUP

3.1. Goals and Limitations

We aim to include the physics of the Galactic magnetic field in the interpretation of observed superbubbles. The derivation of physical quantities from the data, such as the scale height of the surrounding medium or the age of a superbubble is best served by a model that takes into account the magnetic field, but not the complications of a preprocessed interstellar medium. We do not include the effect of Galactic differential rotation or a Coriolis force on the superbubble in our simulations. Tomisaka (1998) found that the characteristic time scale for shear from differential Galactic rotation is ~ 320 Myr while the time scale for shear due to rotation of the bubble by the Coriolis force is ~ 50 Myr. These processes operate over significantly longer times scales than those considered here (up to 20 Myr).

The evolution of the bubble will also be affected by heating and cooling processes. In this paper we discuss adiabatic simulations as an approximation of the situation where heating balances cooling throughout the life of the superbubble, while we use simulations with cooling to explore how the evolution changes if cooling dominates over heating. Observations of ionized gas associated with superbubble shells indicate that a significant fraction of the mass in the shell may be photo-ionized by the central star cluster and the surrounding interstellar radiation field. The ionized mass in the shell of the Orion-Eridanus superbubble is $7 \times 10^4 d_{400}^2 M_\odot$ (Reynolds & Ogden 1979). The neutral mass of this shell was determined to be $5.2 \times 10^5 d_{400}^2 M_\odot$ by Heiles (1976), and $2.5 \times 10^5 d_{400}^2 M_\odot$ by Brown et al. (1995). These values indicate that 13 to 28% of the mass of the Orion-Eridanus shell is ionized by the stars inside the bubble. Pidopryhora et al. (2007) found equal amounts of neutral and ionized gas in the Ophiuchus superbubble, that is possibly ionized from the outside as well as from the inside. The shell of the W4 superbubble (Normandeau et al. 1996) is clearly visible by its thermal radio continuum emission and $H\alpha$ emission (Dennison et al. 1997), but not in HI. Photo-ionization of a substantial fraction of the mass of the shell indicates that heating by photoionization is a non-negligible term in the energy budget of the gas in the shell. Simulations that include cooling without photo-ionization therefore neglect a significant heating term in the energy budget of the shell. For computational reasons we cannot solve radiative transport in the three-dimensional MHD simulations. The absence of cooling in our current simulations corresponds with the approximation of equilibrium between heating and cooling in the shell. In Section 7 we discuss the effect of cooling on the axial ratios of the cavity.

3.2. Basic Equations

Numerical simulations of bubbles have been performed by many researchers (see Robinson et al.

TABLE 1
DIMENSIONLESS PARAMETER CONVERSION

Parameter	Variable	Conversion
Density	ρ	$\tilde{\rho}\rho_0$
Location	x	$\tilde{x}H$
Velocity	\mathbf{v}	$\tilde{\mathbf{v}}c_s$
Time	t	$\tilde{t}H/c_s$
Luminosity	L	$\tilde{L}\rho_0 H^2 c_s^3$
Pressure	p	$\tilde{p}\rho_0 c_s^2$
Internal Energy	e	$\tilde{e}\rho_0 c_s^2$
Magnetic Field	\mathbf{B}	$\tilde{\mathbf{B}}\beta^{-1/2}\rho_0^{1/2}c_s$

TABLE 2
INPUT PARAMETERS

Atmosphere	Source
ρ_0	L_s
β_0	v_s
$\mathbf{B}:(B_1, B_2, B_3)^a$	R_s
Density profile ^b	t_{on}
	t_{off}
	Location: (x_1, x_2, x_3)

^a In the simulations presented here the initial magnetic field is oriented along the x_1 axis ($B_2 = B_3 = 0$), parallel to the Galactic plane.

^b Exp \equiv Exponential according to Equation 14; DL \equiv Dickey & Lockman (1990) according to Equation 15, both with density gradient along the x_2 axis

(2004), Komljenovic et al. (1999), Tomisaka (1998), Mineshige et al. (1993), Mac Low et al. (1989) and Tomisaka & Ikeuchi (1986), among others). Tomisaka (1998) was the first to perform three-dimensional MHD simulations with radiative cooling assuming symmetry with respect to the $x=0$, $y=0$ and $z=0$ planes. In the simulations we present here, we have a complete three-dimensional bubble evolving in an unperturbed, three-dimensional environment.

Our simulations solve the following equations:

$$\frac{\partial \rho}{\partial t} + \nabla \cdot (\rho \mathbf{v}) = 0 \quad (7)$$

$$\frac{\partial \mathbf{B}}{\partial t} - \nabla \times (\mathbf{v} \times \mathbf{B}) = 0 \quad (8)$$

$$\rho \left[\frac{\partial \mathbf{v}}{\partial t} + (\mathbf{v} \cdot \nabla) \mathbf{v} \right] - \nabla p - \rho \nabla \Phi + \frac{(\nabla \times \mathbf{B}) \times \mathbf{B}}{4\pi} = 0 \quad (9)$$

$$\rho \left[\frac{\partial e}{\partial t} + (\mathbf{v} \cdot \nabla) e \right] + p (\nabla \cdot \mathbf{v}) = 0 \quad (10)$$

$$\nabla \cdot \mathbf{B} = 0 \quad (11)$$

where ρ is the density, p is the gas pressure, \mathbf{B} is the magnetic field, \mathbf{v} is the velocity, Φ is the gravitational potential, and e is the internal energy of the gas.

For our simulations we work in units of density (ρ_0), scale height (H) and sound speed (c_s). The conversion to dimensionless variables takes the following form

$$\rho = \tilde{\rho}\rho_0. \quad (12)$$

The other parameters are converted in a similar manner (see Table 1). The unit of time in our simulations is

$$t_0 = \frac{H}{c_s} \quad (13)$$

which is different from the unit of time in the Kompaneets model $t_{0,k}$ in Equation (5), which assumes $c_s = 0$.

The MHD equations in dimensionless variables are solved numerically by the ZEUS-MP code (Norman 2000). The ZEUS-MP code used in this work is an adapted and modified version of the original 1.0b version of Norman and Li (see Norman 2000). One of the authors involved in this paper (R. Ouyed) has also spent a large amount of time to modify the code. Most of these modifications were similar to those described in Vernaleo & Reynolds (2006). A detailed description of the original ZEUS code can be found in Stone & Norman (1992a&b) which also includes basic tests of the code. Vulnerabilities in the ZEUS family noted by Falle (2002), in particular the issue of rarefaction waves and shock errors, have recently been discussed by Hayes et al. (2006; and references therein). While these papers acknowledge that the code possess limitations as do all numerical methods, results from ZEUS-MP were found to compare quite favorably with other numerical techniques. We come to the same conclusion in § 4.3.2 where we compare our results to that of Tomisaka (1998) despite differences in numerical methods used.

ZEUS solves the MHD equations using the operator split method. The equations are solved in two sub-steps, called a source step and a transport step (see Stone & Norman 1992a&b). Three methods for the advection of mass, momentum and internal energy in the transport step can be implemented: the first order accurate donor cell method (Godunov 1959), the second order van Leer method (Van Leer 1977), and the third order piecewise parabolic advection (PPA) method (Colella & Woodward 1984). After some numerical experiments we decided to use the van Leer method because it offers the best ratio of precision to computational costs. The basic equations of the code are written in a covariant form which allows for the use of the code in an arbitrary orthogonal coordinate system (Cartesian, cylindrical and spherical coordinates are predefined). The algorithm used to guarantee that $\nabla \cdot B = 0$ is the “HSMOCC” method which combines the constrained transport (CT) module of Evans & Hawley (1988), and improvements of the method of characteristics (MOC) introduced by Hawley & Stone (1995). In this scheme, if the initial B has zero divergence in the discretisation on the staggered mesh, then every time step will maintain the initial value of the divergence to the accuracy of machine round-off error.

The finite difference method is based on the discretization of each dependent variable over the spatial computational domain. Then finite difference approximations to the differential equations are solved on this discrete mesh. The ZEUS code uses a staggered mesh built up of two mutually shifted grids. The a-grid specifies positions of the zone boundaries while the b-grid specifies the zone centers. Discrete values of all dependent variables are stored for each zone. Scalars are stored at the zone centers while components of vectors are stored at

the appropriate zone interfaces (see Figure 1 in Stone & Norman 1992a). Boundary conditions are implemented as two layers of ghost zones at each boundary of the computational domain (two layers are required for higher order interpolation if the PPA method is used). Values of the dependent variables in the ghost zones are given by simple, explicit equations that connect these values to the values in the adjacent active zones. For our simulations we use the so-called outflow boundary conditions where the values of all variables in the ghost zones are set equal to the values in the corresponding active zones.

The simulations are performed in a three-dimensional cartesian box with right handed coordinates x_1 , x_2 , and x_3 . As initial conditions, we specify a density distribution (atmosphere) and the location of one or more energy sources and their luminosities (as described in the following sections). For a summary of these input parameters refer to Table 2.

3.3. Atmosphere Setup

We consider two functional forms for the distribution of the ambient gas. The first form is an exponential density distribution

$$\tilde{\rho} = \exp[-\tilde{x}_2]. \quad (14)$$

The second form is the density distribution proposed by Dickey & Lockman (1990) (hereafter DL) from their analysis of the vertical distribution of atomic hydrogen in the Galaxy. This density distribution, in terms of dimensionless variables, is

$$\begin{aligned} \tilde{\rho} = & \frac{0.395}{0.566} \exp\left[-\frac{1}{2}(a_1\tilde{x}_2)^2\right] + \\ & + \frac{0.107}{0.566} \exp\left[-\frac{1}{2}(a_2\tilde{x}_2)^2\right] + \\ & + \frac{0.064}{0.566} \exp\left[-a_3|\tilde{x}_2|\right] \end{aligned} \quad (15)$$

where $a_1 = 100/90$, $a_2 = 100/225$, and $a_3 = 100/403$. The coefficients a_i express the scale heights of the three components of the DL layer in units of 100 pc. Contrary to the exponential profile, the DL layer has an equatorial plane, $\rho(x_2 = 0) = 1$, with density decreasing in both the positive and negative x_2 directions. This is the same density distribution adopted by Tomisaka (1998).

The dynamical importance of the magnetic field is set through the parameter β_0 , defined as the ratio between the gas pressure and magnetic pressure at $x_2 = 0$

$$\beta_0 = \frac{8\pi p}{B^2} \quad (16)$$

The magnetic field strength is

$$\begin{aligned} B = & \left(\frac{8\pi p}{\beta_0}\right)^{1/2} = \\ 5.0 & \left(\frac{\rho}{1.67 \times 10^{-24} \text{ g cm}^{-3}}\right)^{1/2} \beta_0^{-1/2} \mu\text{G} \end{aligned} \quad (17)$$

where the numeric expression was derived using $c_s^2 = \gamma p / \rho$.

We consider two geometries of the magnetic field. The first is a constant field, i.e. the vertical scale height of the magnetic field is infinite ($B(x_2) = B_0$), the other takes

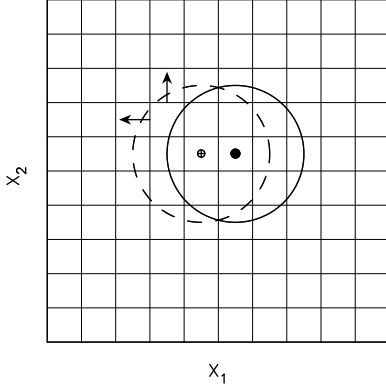


FIG. 1.— The oscillation of the source in x_1 , x_2 , and x_3 results in a nearly isotropic source with radius only a few zones. The dashed circle represents the idealized spherical source at one time, the solid circle represents the idealized source at another time. Horizontal and vertical lines represent zone boundaries. The two arrows illustrate velocity vectors for two locations on the a-grid where mass outflow from the source occurs when the idealized source is represented by the dashed circle. In the simulations, the amplitude of the oscillation is set to only half a zone.

the scale height of the magnetic pressure to be equal to the scale height of the gas pressure ($\beta = \beta_0$ everywhere). We refer to the constant β case as equipartition although strictly speaking equipartition implies $\beta = 1$ everywhere. The scale height of the Galactic magnetic field is not well known. Our initial conditions cover the possibility of a large scale height $\gtrsim 1$ kpc corresponding to a magnetically dominated halo, and a small scale height (equal to $2H$ for an exponential atmosphere). Hydrostatic equilibrium is assured by imposing a gravitational potential that balances the gradient of the total pressure which is the sum of the gas pressure and the magnetic pressure. The maintenance of hydrostatic equilibrium was tested in simulations with no source for both atmospheres. The vertical velocity in these tests was less than $10^{-4}c_s$ after 10 Myr simulated time. This is consistent with numerical errors and it has no effect on the results of our simulations.

3.4. The Energy Source

The source of the bubble is defined by its mechanical luminosity (L_s) related to the mass loss rate (\dot{m}_s) and the outflow velocity (v_s) according to

$$L_s = \frac{1}{2} \dot{m}_s v_s^2. \quad (18)$$

The source is assigned a finite radius (R_s), determined by the spatial resolution of the simulation. The mass loss rate from the source is related to the outflow velocity and the radius of the source via

$$\dot{m}_s = \rho_s v_s 4\pi R_s^2. \quad (19)$$

Solving for ρ_s and converting to dimensionless variables, we find

$$\tilde{\rho}_s = \frac{\tilde{L}_s}{2\pi \tilde{R}_s^2 \tilde{v}_s^3} \quad (20)$$

Values for \tilde{R}_s , \tilde{L}_s and \tilde{v}_s are specified as initial conditions. At every time step, $\tilde{\rho}_s$ and \tilde{v}_s are reset to their initial values to maintain constant momentum and energy input from the source. To simulate a point source,

TABLE 3
PHYSICAL PARAMETERS FOR SIMULATIONS PERFORMED:
SOURCE AND ATMOSPHERE

Simulation	L_s (10^{37} erg s $^{-1}$)	n_0 ($z = 0$) (cm $^{-3}$)	B	β_0
Constant Atmosphere				
ConstH_zoom	3	1	no B	∞
ConstH	3	1	no B	∞
ConstMHD	3.2	0.32	const	1.16
Exponential Atmosphere				
ExpH_zoom	3	1	no B	∞
ExpH	3	1	no B	∞
ExpCBa	3	1	const	10
ExpCBb	3	1	const	3
ExpCBc	3	1	const	1
ExpCBd	3	1	const	0.3
ExpEBa	3	1	equip	10
ExpEBb	3	1	equip	3
ExpEBc	3	1	equip	1
ExpEBd	3	1	equip	0.3
DL Atmosphere				
DLH	3	1	no B	∞
DLCBa	3	1	const	10
DLCBb	3	1	const	3
DLCBc	3	1	const	1
DLCBd	3	1	const	0.3
DLEBa	3	1	equip	10
DLEBb	3	1	equip	3
DLEBc	3	1	equip	1
DLEBd	3	1	equip	0.3
Tomisaka A	3	0.3	const	0.7

the radius R_s should be taken as small as possible. However, in the rectangular grid, the outflow from the source will be more isotropic if R_s is more than a few times the grid size. A complication is that density is evaluated in the center of a pixel (b-grid), whereas velocity is evaluated on the boundary of a pixel (a-grid). This is part of a strategy to conserve mass in the simulations, but it introduces an asymmetry in the radius of a sphere when coordinates are rounded off to integer multiples of the grid size. To maintain an isotropic source while avoiding computationally intensive interpolations that must be performed every time step, the location of the source is oscillated in three dimensions by half a grid position every time step (see Figure 1). These excursions of the source along the three axes are incoherent, and average out most of the anisotropy introduced by the numerical grid for small R_s . The isotropy of the source setup was tested in hydrodynamic simulations with no density gradient. These experiments showed that R_s between two and three pixels results in good symmetry in the simulations. A small degree of anisotropy in the outflow of the source remains. This acts as a seed for the development of instabilities, but is not considered a problem for our analysis.

4. RESULTS

The simulations were performed on the CAPCA¹ computer cluster which consists of 64 2.4 GHz Linux based

¹ Computational Astro-Physics Calgary Alberta
(www.capca.ucalgary.ca)

processors connected by a 1 gigabit network. The results of these simulations were analyzed using JETGET (Staff et al. 2004) and KVIS, a program that is part of the Karma visualization package (Gooch 1996).

In the simulations that we present here, we examined the effects of magnetic field strength and geometry on the evolution of a superbubble in the two atmospheres defined in Section 3.3. The other parameters were fixed to the values in Table 3 to apply our simulations to published results on the bubble associated with the W4 region as described by Normandeau et al. (1996) and Basu et al. (1999) (Section 5). Table 3 gives a summary of the simulations and the values of the varied physical parameters. Table 4 gives details on the simulation volume. To test convergence we ran simulations at 100^3 , 200^3 and 300^3 zones and established convergence at 200^3 which corresponds to a resolution of 5 pc per voxel (see Section 4.4.1).

4.1. Comparison to Analytical Solutions

4.1.1. Hydrodynamic Solutions

In order to test the setup, we performed hydrodynamic simulations with a constant density profile (ConstH_{zoom} & ConstH) to compare with the Castor et al. (1975) model and a hydrodynamic simulation with an exponential density profile (ExpH_{zoom}) to compare with the K60 model. The physical parameters for these simulations are given in Table 3. Maintaining the same number of pixels for a smaller volume (300 pc on a side) results in a finer resolution (1.5 pc compared to the 5 pc resolution of the other simulations listed in Table 4). This allows us to follow the evolution of the bubble in detail at early times. We have multiple reasons to consider high-resolution simulations for the comparison with the Castor et al. (1975) and K60 models. The first reason is to investigate the effect of resolution on our solutions. The second reason is to explore the effect of the finite source size. In our simulations, the bubble begins at a finite radius at $t = 0$ (the radius of the source) which can be made smaller in high resolution simulations. Although the Castor et al. (1975) model is self-similar, increasing the resolution will allow us to investigate the effect of the finite source size in the simulations at early times. The K60 model is not self-similar, but it is only expected to agree with the simulations at early times (Section 2).

Both models assume that the sound speed in the ambient medium is zero by assuming the pressure in the undisturbed medium is negligible. For our simulations, the sound speed in the undisturbed medium is finite, but the assumption of negligible pressure is satisfied as long as the pressure inside the bubble is much larger than the pressure of the surrounding atmosphere. The limit of negligible ambient pressure adopted in the K60 model implies $t_o \gg t_{ok}$. In our simulations, the time scale t_o (Equation 13) is $\sim 10^7$ years, whereas the timescale t_{ok} of the K60 model (Equation 5) is $\sim 0.05 \times 10^7$ years. The simulations should therefore resemble the Kompaneets model at times much less than 10^7 years.

The size of the bubble was parameterized by the radius of the contact discontinuity, which is well defined in both the simulations and the Kompaneets model. The

shell of swept-up interstellar medium is presumed to be infinitely thin in the Kompaneets model, so the radius of the outer shock is not predicted. For consistency, the same was done for the spherical case. The radius of the contact discontinuity for the spherical model was taken to be 86% of the outer shock radius following Weaver et al. (1977). For ConstH_{zoom}, the contact discontinuity is located at 84% of the outer shock radius, which is in good agreement with the Weaver et al. (1977) model. Figure 2A compares the time evolution of the radius of ConstH_{zoom} with the spherical model. The simulation displays a power law expansion with time $R_b \sim t^\alpha$ with $\alpha = 0.566$. This is only 5.7% smaller than the slope of the Castor et al. (1975) model, which has $\alpha = 0.6$. At an age of 1 Myr the radius of ConstH is 9% larger than the radius of the model. The filled squares in Figure 2A show the time evolution of ConstH. The radius of the bubble in this simulation is at most 10% larger than the radius in the higher resolution simulation at the same age. This indicates that part of the difference between our simulations and the Castor model may be related to the finite size of the source.

Figure 2B shows the time evolution of the radius² of a bubble in an exponential atmosphere (ExpH_{zoom} in Tables 3 and 4), looking perpendicular to the Galactic plane, for the simulations and the K60 model. Also shown is the spherical model from Figure 2A as a reference line. The bottom of the simulation closely follows the K60 model. However the top of the K60 model is consistently higher than the simulation by about 16% even at early times. This is also shown in Figure 3. As time proceeds, the difference between the K60 model and the simulations increases significantly at the top of the bubble but not at the bottom. Komljenovic et al. (1999) also compared their 2-dimensional hydrodynamic simulations to the Kompaneets model with similar results. Mac Low et al. (1989) found consistency between their Kompaneets approximation from Mac Low & McCray (1988) and hydrodynamic simulations at times as late as 6.87 Myr. However, their Kompaneets approximation is a solution in an atmosphere with an equatorial plane unlike the Kompaneets model (Kompaneets 1960) considered here. The axial ratio in the Galactic plane (i.e. x_1x_3) is expected to be unity at all times for the hydrodynamic case and also at early times in the MHD case (see Section 4.4). The radius of the cross-section through the source of the K60 model as a function of time can be calculated to a good approximation from the spherical Castor model, as shown numerically by Basu et al. (1999).

4.1.2. MHD Analytical Approximation

Ferrière et al. (1991) derived analytic solutions of a superbubble in a uniform magnetic field in the limit of high expansion velocity, and numerical solutions for the general case of smaller expansion velocity. To compare with their solutions, we ran an MHD simulation in an atmosphere with constant density (ConstMHD, see Tables 3 & 4). Ferrière et al. (1991) found that the outer shock

² Here, the radius is defined separately for each direction as the distance from the source to the contact discontinuity at the top of the bubble and the distance from the source to the contact discontinuity at the bottom of the bubble.

TABLE 4
BOX PARAMETERS FOR SIMULATIONS PERFORMED: VOLUME SETUP^a

Simulation	$x_1 \times x_2 \times x_3$ pc \times pc \times pc	$(x_1 \& x_3)_{min-max}$ H	$(x_2)_{min-max}$ H	$n_{x_1} \times n_{x_2} \times n_{x_3}$ zones \times zones \times zones
Constant Atmosphere				
ConstH _{zoom}	$300 \times 300 \times 300$	-1.5 to 1.5	-1 to 2	$200 \times 200 \times 200$
ConstH	$10^3 \times 10^3 \times 10^3$	-5 to 5	-3 to 7	$200 \times 200 \times 200$
ConstMHD	$10^3 \times 10^3 \times 10^3$	-5 to 5	-5 to 5	$200 \times 200 \times 200$
Exponential Atmosphere				
ExpH _{zoom}	$300 \times 300 \times 300$	-1.5 to 1.5	-1 to 2	$200 \times 200 \times 200$
ExpH	$10^3 \times 10^3 \times 10^3$	-5 to 5	-3 to 7	$200 \times 200 \times 200$
ExpCBa	$10^3 \times 10^3 \times 10^3$	-5 to 5	-3 to 7	$200 \times 200 \times 200$
ExpCBb	$10^3 \times 10^3 \times 10^3$	-5 to 5	-3 to 7	$200 \times 200 \times 200$
ExpCBc	$10^3 \times 10^3 \times 10^3$	-5 to 5	-3 to 7	$200 \times 200 \times 200$
ExpCBd	$10^3 \times 10^3 \times 10^3$	-5 to 5	-3 to 7	$200 \times 200 \times 200$
ExpEBa	$10^3 \times 10^3 \times 10^3$	-5 to 5	-3 to 7	$200 \times 200 \times 200$
ExpEBb	$10^3 \times 10^3 \times 10^3$	-5 to 5	-3 to 7	$200 \times 200 \times 200$
ExpEBc	$10^3 \times 10^3 \times 10^3$	-5 to 5	-3 to 7	$200 \times 200 \times 200$
ExpEBd	$10^3 \times 10^3 \times 10^3$	-5 to 5	-3 to 7	$200 \times 200 \times 200$
DL Atmosphere				
DLH	$10^3 \times 10^3 \times 10^3$	-5 to 5	-5 to 5	$200 \times 200 \times 200$
DLCBa	$10^3 \times 10^3 \times 10^3$	-5 to 5	-5 to 5	$200 \times 200 \times 200$
DLCBb	$10^3 \times 10^3 \times 10^3$	-5 to 5	-5 to 5	$200 \times 200 \times 200$
DLCBc	$10^3 \times 10^3 \times 10^3$	-5 to 5	-5 to 5	$200 \times 200 \times 200$
DLCBd	$10^3 \times 10^3 \times 10^3$	-5 to 5	-5 to 5	$200 \times 200 \times 200$
DLEBa	$10^3 \times 10^3 \times 10^3$	-5 to 5	-5 to 5	$200 \times 200 \times 200$
DLEBb	$10^3 \times 10^3 \times 10^3$	-5 to 5	-5 to 5	$200 \times 200 \times 200$
DLEBc	$10^3 \times 10^3 \times 10^3$	-5 to 5	-5 to 5	$200 \times 200 \times 200$
DLEBd	$10^3 \times 10^3 \times 10^3$	-5 to 5	-5 to 5	$200 \times 200 \times 200$
Tomisaka A	$10^3 \times (2 \times 10^3) \times 10^3$	0 to 10	-10 to 10	$200 \times 400 \times 200$

^a This table gives information on the main set of simulations. Additional simulations for convergence tests with $100 \times 100 \times 100$ and $300 \times 300 \times 300$ zones (see Figure 10) are not listed.

front remains nearly spherical in a uniform magnetized medium, but the cavity is smaller in the direction perpendicular to the magnetic field, compared with the hydrodynamic solution. We find the same in our numerical simulation, but we see no dimple in the outer shock in the direction of the magnetic field. Tomisaka (1998) also did not see this dimple. The expansion along the magnetic field lines is nearly the same as in the hydrodynamic simulation as found by Ferrière et al. (1991).

The thickness of the shell perpendicular to the magnetic field in the analytic approximation found by Ferrière et al. (1991), increases linearly with time according to

$$\Delta R = 1.2 \frac{B_{-6} t_6}{\sqrt{n_0}} \sin \theta \text{ pc} \quad (21)$$

where n_0 is the number density in cm^{-3} , B_{-6} is the ambient magnetic field strength in μG , and t_6 is the time in Myr. Our simulation reproduces the linear increase of shell thickness perpendicular to the magnetic field with time, but the shell thickness is a factor ~ 2.6 larger. The simulations by Tomisaka (1998) also show a very thick shell perpendicular to the magnetic field, although he did not consider a medium with constant density. The reason for the difference is that Equation (21) was derived in the limit of high expansion velocity, defined as a small ratio of magnetic pressure to ram pressure. This ratio increases with time as the outer shock decelerates. We find that this ratio is of order unity or larger at times $\gtrsim 2.5$ Myr in our simulation. Simulations with higher

β reproduce the shell thickness in Equation (21), while also satisfying the assumptions made in the derivation of this equation.

4.2. Exponential Atmosphere

4.2.1. Model ExpH

A simulation of a bubble expanding in an exponential atmosphere with no magnetic field was done primarily to compare with previously published results and to obtain the limiting case $\beta = \infty$. At early times, the bubble remains spherical (Figure 3). The axial ratio of the cavity in the simulations *and the axial ratio of the Kompaneets model* are indeed found to be very close to unity, even though Figure 3 shows that the top of the Kompaneets model has proceeded significantly further than the simulation even at these early times. In Appendix A we show that the Kompaneets model at early times can be described to third order in \tilde{y} as a spherical cavity that rises in the atmosphere. Although the axial ratio remains unity to a high degree of accuracy, the geometric center of the model, defined by the point midway between the top and the bottom (crosses in Figure 3), is displaced significantly from the location of the source.

At later times, the bubble grows larger than the scale height of the medium and accelerates in the vertical direction. As the bubble expands into the upper atmosphere, the top of the bubble continues to accelerate and a Rayleigh-Taylor instability develops when the top reaches ~ 4 scale heights above the source, which occurs

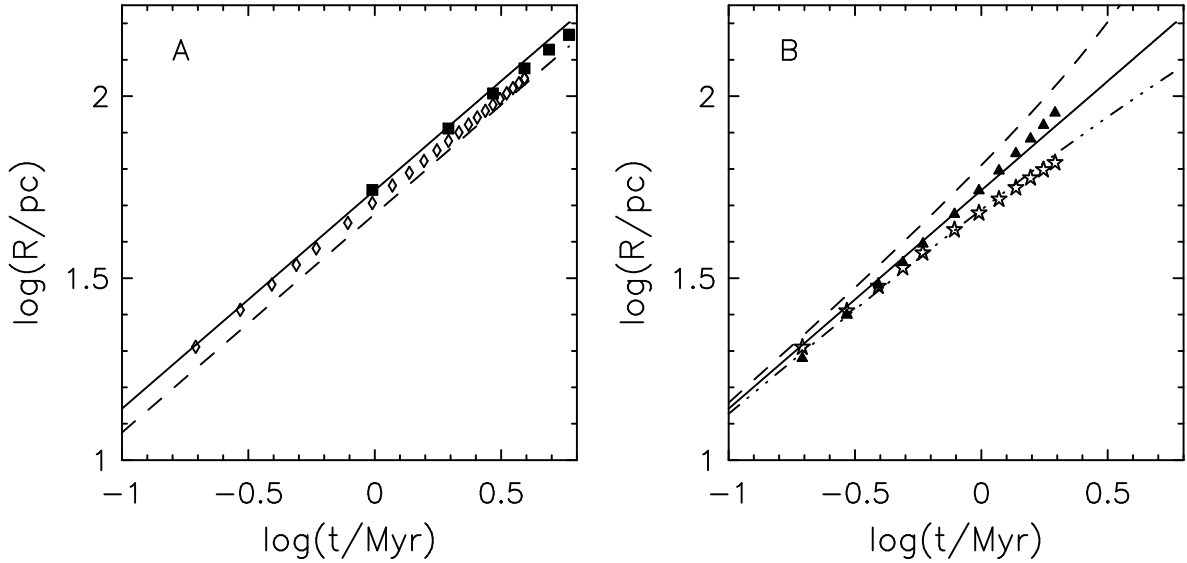


FIG. 2.— (A) Time evolution of the radius of a stellar wind bubble in a medium with constant density and no magnetic field. Diamonds show the radius of the bubble in a simulation with $200 \times 200 \times 200$ zones that measures $300 \times 300 \times 300$ pc (i.e. a resolution of 1.5 pc per voxel). Squares show the radius of a bubble in a $200 \times 200 \times 200$ simulation that measures $1000 \times 1000 \times 1000$ pc (i.e. a resolution of 5 pc per voxel). In both cases the radius of the source was 2 pixels. The radii of the simulations are compared with the radius of the contact discontinuity in the Weaver et al. (1977) model (dashed line). Also shown is the radius of the outer shock in the Weaver et al. (1977) model (solid line). (B) Time evolution of the radius of the bubble in an exponential atmosphere in the positive x_2 direction (filled triangles) and the negative x_2 direction (stars). The corresponding radii from the K60 model are shown as a dashed curve and a dot-dashed curve respectively. Also shown is the Weaver et al. (1977) constant density model from panel A (solid line). See Appendix A for a discussion on the difference between the simulations and the K60 model at early times.

at an age of ~ 10 Myr. The bubble breaks out of the galactic plane to form a chimney after about 16 to 17 Myr.

4.2.2. Models *ExpCB(a-d)* & *ExpEB(a-d)*

The main difference between a constant magnetic field and equipartition magnetic field is in the evolution of the bubble at large distances from the Galactic plane. A constant magnetic field implies a high Alfvén speed in the Galactic halo whereas constant β implies that the Alfvén speed in the halo is the same as in the disk. This difference has significant consequences for the structure of the shock as it expands from the disk into the halo. Figure 4 shows a bubble in an exponential atmosphere with constant magnetic field ($\beta_0 = 1$) oriented along the x_1 axis, at an age of 10 Myr.

The cavity is elongated along the magnetic field as the plasma can move freely along the field lines but its motion perpendicular to the field lines is restricted. However, the shape of the outer shock at the level of the source in the Galactic plane (x_1x_3 plane) is nearly circular because the propagation speed of the outer shock is similar in both directions. Along the x_1 axis, the outer shock and the contact discontinuity are close together resulting in a thin compressed shell of swept-up interstellar medium. Along the x_3 axis, perpendicular to the initial magnetic field, the distance between the outer shock and the contact discontinuity is much larger resulting in a thick shell. Looking along the field lines, the cavity is more elongated than in the hydrodynamic simulation, and the shell of swept-up interstellar medium is thicker than in the hydrodynamic case. At the top of the cavity a fast magnetosonic wave runs upwards into

the halo, with very little compression of the halo gas. In contrast to the hydrodynamic simulation, we see no evidence for a Rayleigh-Taylor instability developing at the top of the bubble, because the top of the bubble does not accelerate. Instead, an instability develops everywhere at the contact discontinuity as is apparent from the scalloped shape of the contact discontinuity in the x_3x_2 plane (looking along the field lines). This instability also occurs in the simulations of Tomisaka (1998) and may be similar to the magnetically enhanced Rayleigh-Taylor instability proposed by Gregori et al. (2000). At the time shown in Figure 4, the expansion of the cavity along the x_3 axis (perpendicular to the magnetic field) in the Galactic plane has stalled as a result of magnetic tension. The cavity still expands along the x_1 and x_2 axes.

Figure 5 shows simulation *ExpEBc* also at the age of 10 Myr. In contrast with Figure 4, Figure 5 shows a shell of compressed interstellar medium at the top of the bubble. Since the Alfvén velocity does not increase with distance from the Galactic plane, the outer magnetosonic shock does not accelerate into the halo but remains close to the contact discontinuity. The shell appears approximately twice as thick looking along the field lines as looking perpendicular to the magnetic field. The axial ratio of the cavity in the x_3x_2 plane (looking along the field lines) is smaller than in the *ExpCBc* simulation. This indicates the importance of magnetic tension confining the bubble, even though the total pressure mimics the pressure in the hydrodynamical exponential atmosphere. The magnetic field in the upper part of the shell is significantly enhanced compared to the magnetic field in the undisturbed atmosphere at the same height above the

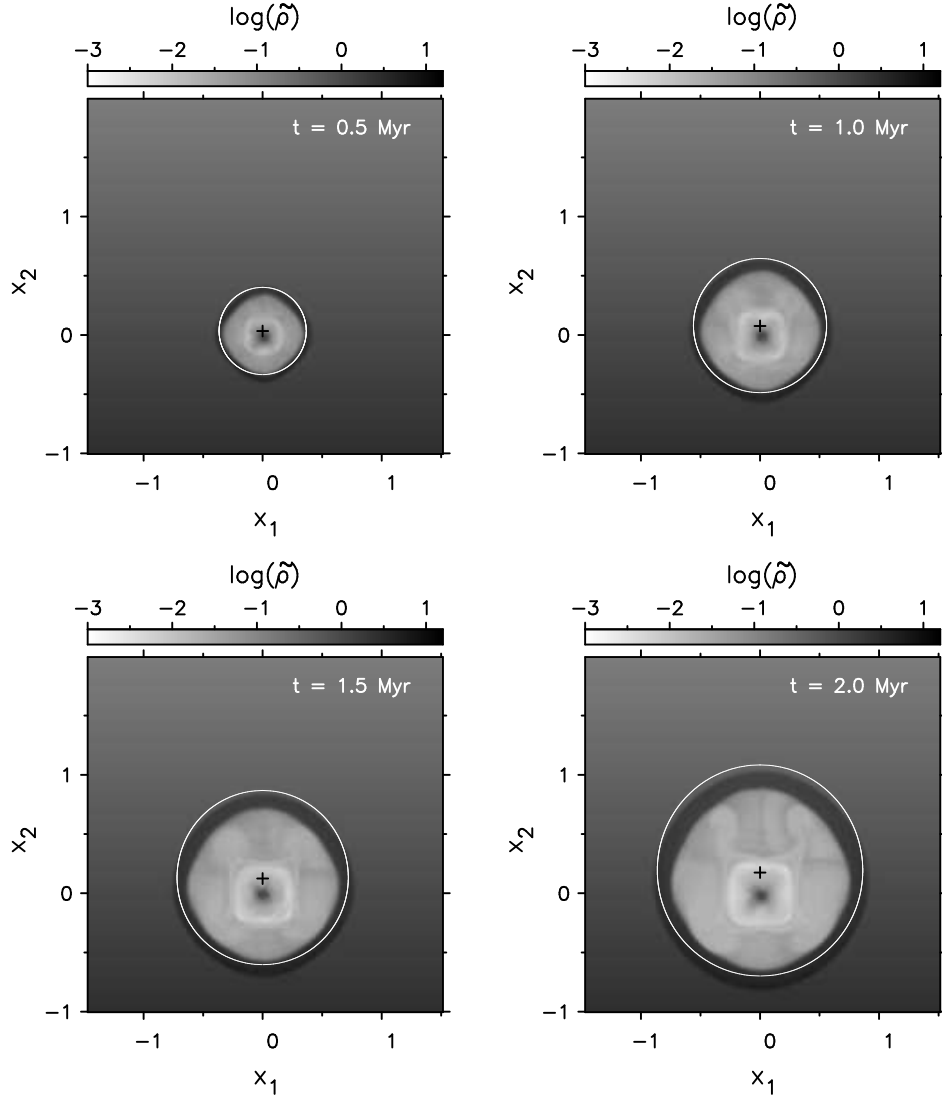


FIG. 3.— Early stages of a zoomed-in hydrodynamic simulation with Kompaneets solution overlaid (white circles) in a plane through the centre of the source at $(x_1, x_2, x_3) = (0, 0, 0)$. Gray scales represent density on a logarithmic scale from 10^{-3} to $10^{1.2} \text{ cm}^{-3}$. At early times, the Kompaneets model is nearly spherical, but the center of the sphere has a visible offset in the direction of the density gradient (see Appendix A). The geometric center of the Kompaneets solution as defined in Appendix A is shown as a + in each panel. The values for \tilde{y} (Equation 4) are 0.36, 0.55, 0.70, and 0.84 for these panels in increasing time order. The unit of length on the axes is 100 pc.

plane. Here too, we see an instability everywhere along the contact discontinuity in the x_3x_2 plane.

4.3. Dickey & Lockman Atmosphere

4.3.1. Model DLH

The simulations in the DL atmosphere show some differences compared to the evolution in the exponential atmosphere. The equatorial plane introduces symmetry with respect to the plane $x_2 = 0$. In the absence of a magnetic field the bubble is spherical until it expands to radius ~ 200 pc. Once the radius of the bubble grows beyond ~ 200 pc, it becomes more elongated in the vertical direction as it balloons out into the halo (Figure 6). The top and bottom of the bubble expanding into the low-density outer atmosphere, accelerate away from the Galactic plane, as in the case of an exponential atmosphere. The onset of a Rayleigh-Taylor instability is not seen in this simulation but it may develop at later times outside the simulation volume.

Between an age of ~ 14 Myr and ~ 18 Myr a small decrease in the radius of the cavity in the equatorial plane is observed. A similar stall of the expansion and subsequent contraction in the Galactic plane triggered by the rapid vertical expansion of the bubble was observed by Tomisaka (1998).

4.3.2. Models DLCB(a-d) & DLEB(a-d)

Figure 7 shows the simulation of a bubble in the DL atmosphere with constant magnetic field oriented along the x_1 axis at an age of 10 Myr. As with the exponential simulations, this simulation shows the same features as discussed by Tomisaka (1998). The cavity is elongated along the magnetic field lines. The shape of the outer shock at the level of the source in the x_1x_3 plane is nearly circular, similar to the exponential case. This is to be expected because the density and magnetic field strengths are the same at the level of the source in both atmospheric profiles. In contrast to the exponential at-

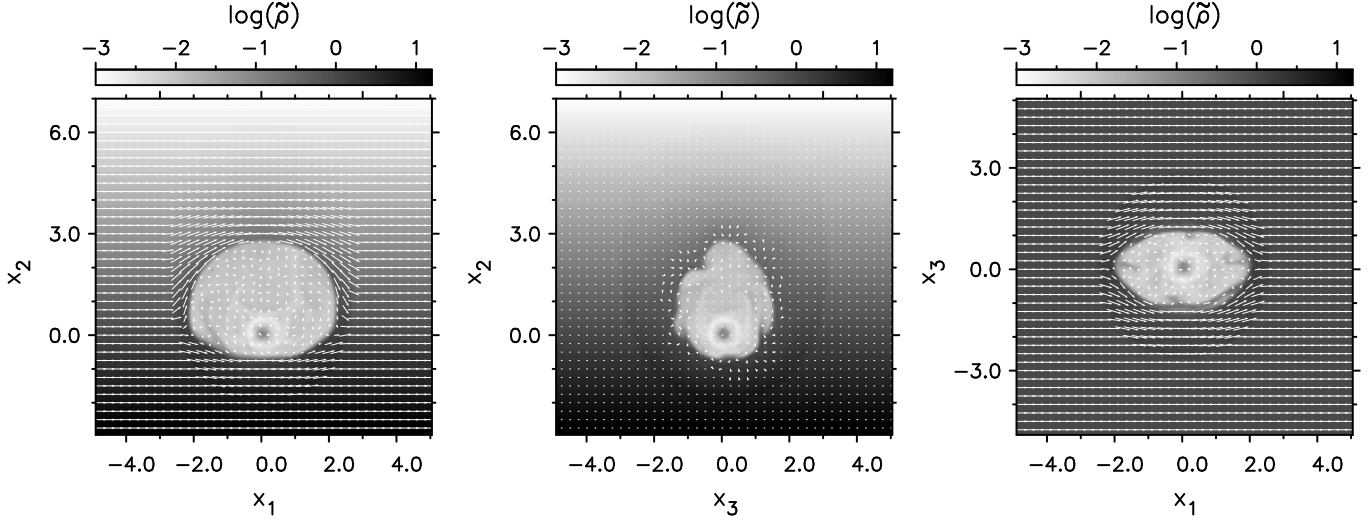


FIG. 4.— Simulation ExpCBc at an age of 10 Myr. Magnetic field initially oriented along x_1 axis, $\beta = 1$. Panels show slices through the cube at the location of the source, $(x_1, x_2, x_3) = (0, 0, 0)$, in three orthogonal planes. Grayscales show the gas density on a logarithmic scale from 10^{-3} (white) to $10^{1.2}$ (black) cm^{-3} . The vector field depicts the projection of magnetic field vectors on the plane of the image. The unit of length on the axes is 100 pc.

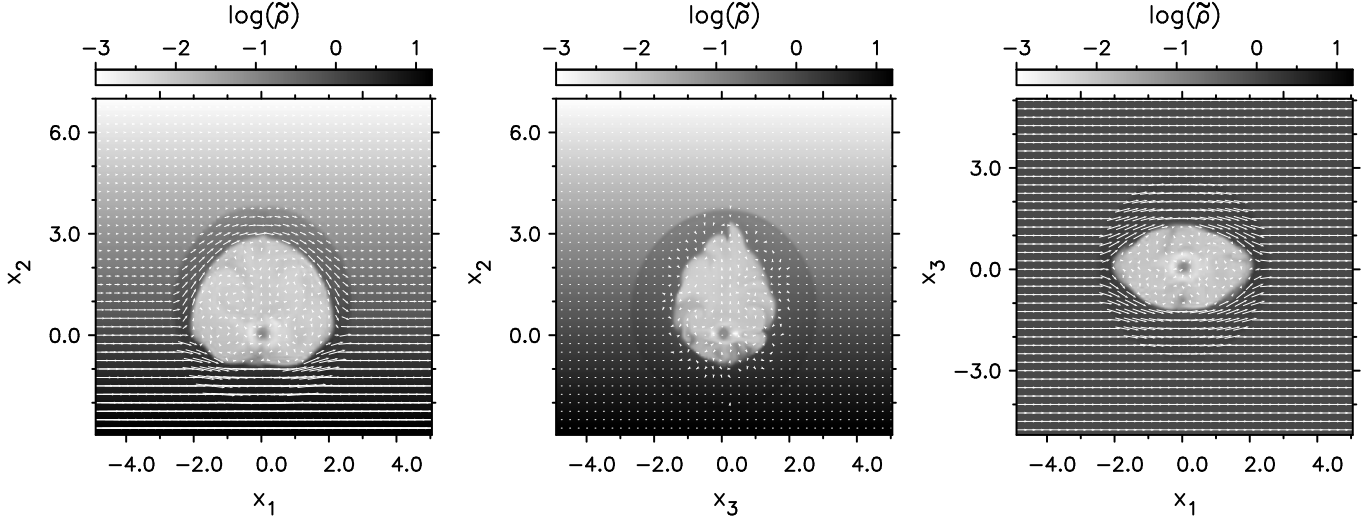


FIG. 5.— Same as Figure 4 but for Simulation ExpEBc at an age of 10 Myr.

mosphere, the shape of the cavity in the x_1x_2 plane is fairly circular even though the bubble expands to a size much larger than the pressure scale height. The shape of the cavity in the x_3x_2 plane is quite elongated and displays the same magnetically enhanced Rayleigh-Taylor instability as discussed in Section 4.2.2. As with the ExpCBc case, a fast magnetosonic wave runs upwards into the halo. Figure 8 shows the constant β simulation DLEBc at the same age. The discussion of the differences between the ExpCBc and ExpEBc applies also to simulations in the DL atmosphere.

We performed an extra simulation (Tomisaka A) in a larger volume to compare with Model A in Tomisaka (1998), with the same equatorial density. Other initial conditions were set as closely as possible to those specified by Tomisaka (1998) (see Tables 3 & 4), but some small differences in the setup could not be avoided. Our simulations show the same characteristics in terms of the size and shape of the cavity, and the thickness of the sur-

rounding shell. However we found differences of the order of 20% in the dimensions of the cavity after 10 Myr which appear to be associated with small differences in initial conditions. The fast magnetosonic shock had proceeded to almost twice the height of the shock in Model A of Tomisaka (1998), indicating a lower value of β in our simulation. The shape of the magnetosonic shock front is particularly sensitive to small differences in β because the Alfvén speed at high altitudes is very sensitive to β .

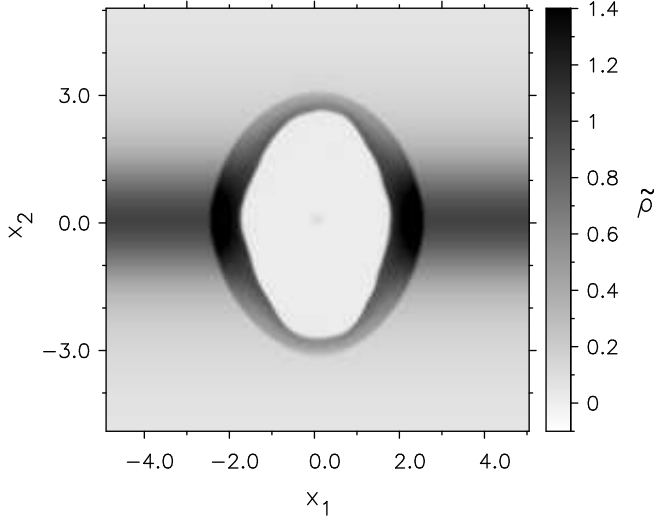


FIG. 6.— Simulation DLH (hydrodynamic) at an age of 10 Myr. The density in a slice through the cube at the location of the source, $(x_1, x_2, x_3) = (0, 0, 0)$, in the x_1x_2 plane is shown with linear grayscale from -0.2 (white) to 1.4 (black) cm^{-3} . The unit of length on the axes is 100 pc.

4.4. Bubble Morphology as a Function of Time and Magnetic Field Strength

Our simulations cover a factor 30 in magnetic field strength, from relatively weak (those labeled with 'a', $\beta = 10$) to strong (those labeled with 'd', $\beta = 0.3$). Here we discuss variation in the shape of a bubble with magnetic field strength at a reference age of 10 Myr. The weak magnetic field limit for the simulations converges to the hydrodynamic case as should be expected. The differences between simulations with $\beta = 10$ and hydrodynamic simulations are minor. We limit the discussion to the range $\beta = 10$ to 0.3.

One of the most visible effects of the magnetic field is on the size of the cavity. A decrease in β by a factor of 30 results in a decrease in the vertical size of the cavity by a factor ~ 1.7 , independent of the density and magnetic field stratifications. The diameter of the cavity in the x_1 direction (along the field lines) increases by a factor of ~ 1.4 as β decreases. Expansion along the magnetic field is faster as the magnetic field is stronger. The diameter of the cavity along the x_3 axis decreases by a factor ~ 1.6 as β decreases from 10 to 0.3. The effect of a stronger magnetic field on the shape of the cavity is that the cavity becomes more elongated along the Galactic plane when observed along a direction perpendicular to the Galactic magnetic field. When observed along the direction of the magnetic field, the shape of the cavity varies less, but the size of the cavity becomes significantly smaller.

The thickness of the shell in the directions perpendicular to the magnetic field also increases dramatically with increasing magnetic field strength. However, this happens at the expense of the amount of compression of gas in the shell, which becomes nearly invisible in the simulations with $\beta = 0.3$. In practice, the shell may not be detectable in real data confused with emission in the foreground and background, even for $\beta = 1$, if the magnetic field scale height is large (see Figure 4). The increasing thickness of the shell along the x_3 axis is partly the result of the smaller extent of the cavity, partly because of a faster expansion of the outer shock, approximately by

equal amounts. In simulations with a constant magnetic field, the thickness of the shell at the top of the bubble increases mainly because of the fast upward expansion of the outer shock, and to a lesser amount by the smaller extent of the cavity. In the equipartition simulations, the increased thickness of the top of the shell is mainly because of the smaller extent of the cavity. Along the magnetic field lines (x_1), the thickness of the shell decreases as the magnetic field strength increases. However, no strong increase in the density is found at the extremes of the shell along the x_1 axis.

Figure 9 compares the time evolution of the semi-major axis of the contact discontinuity and the outer shock in the x_1x_3 plane, for a sample of our simulations (ExpH, DLH, ExpCBc, & DLCBc), with that of the Castor et al. (1975) model. The semi-major axis is defined as half the diameter along the x_1 axis at the level of the source. The expansion along the magnetic field lines at early times (see Figure 9a) closely follows the hydrodynamic solution in accordance with Ferrière et al. (1991). The contact discontinuity of the self-similar solution was found to be at 86% of the shock radius by Weaver et al. (1977). The radius of the contact discontinuity in the analytic model indeed agrees well with the radii of the contact discontinuity in our simulations at early times (dashed curve in Figure 9). At later times (Figure 9b), the contact discontinuity in the ExpCBc and DLCBc simulations has proceeded further than the analytic solution (dashed curve). On the other hand, the contact discontinuity in the ExpH and DLH simulations lags behind the analytic solution. We interpret this behavior as the result of the hydrodynamic simulations breaking out of the disk, reducing the pressure inside the cavity, whereas the MHD simulations remain confined to the disk. We find that the location of the outer shock in these simulations is nearly the same even after 15 Myr in agreement with results presented in Ferrière et al. (1991).

4.4.1. Axial Ratios

The discussion in the previous subsection shows that the magnetic field is as important as the density distribution of the medium in determining the shape of a superbubble. Observationally, the shape of the cavity is most important because structures with a large contrast in density are most easily detected in HI images of the Galaxy.

Figure 10 shows the axial ratio of the low-density cavity in the Galactic plane (x_3/x_1) versus time for different resolutions (100^3 , 200^3 and 300^3) to verify convergence (see Section 4). From this, we confirm that convergence is established at 200^3 which we use for the analysis. Figure 11 shows the relationship between the x_3/x_1 axial ratio and β at an age of 5 Myr and 12.5 Myr. The similarity between the four panels shows that the axial ratio of a superbubble in the Galactic plane does not depend significantly on the vertical stratification of the density and the vertical stratification of the magnetic field (see also Figures 4, 5, 7 and 8). The important parameters are the age of the bubble and the strength of the magnetic field in the equatorial plane. Even at the relatively young age of 5 Myr, a bubble in a medium with $\beta = 1$ will be elongated along the magnetic field with axial ratio ~ 0.8 . After 12.5 Myr, the size of the bubble perpendicular

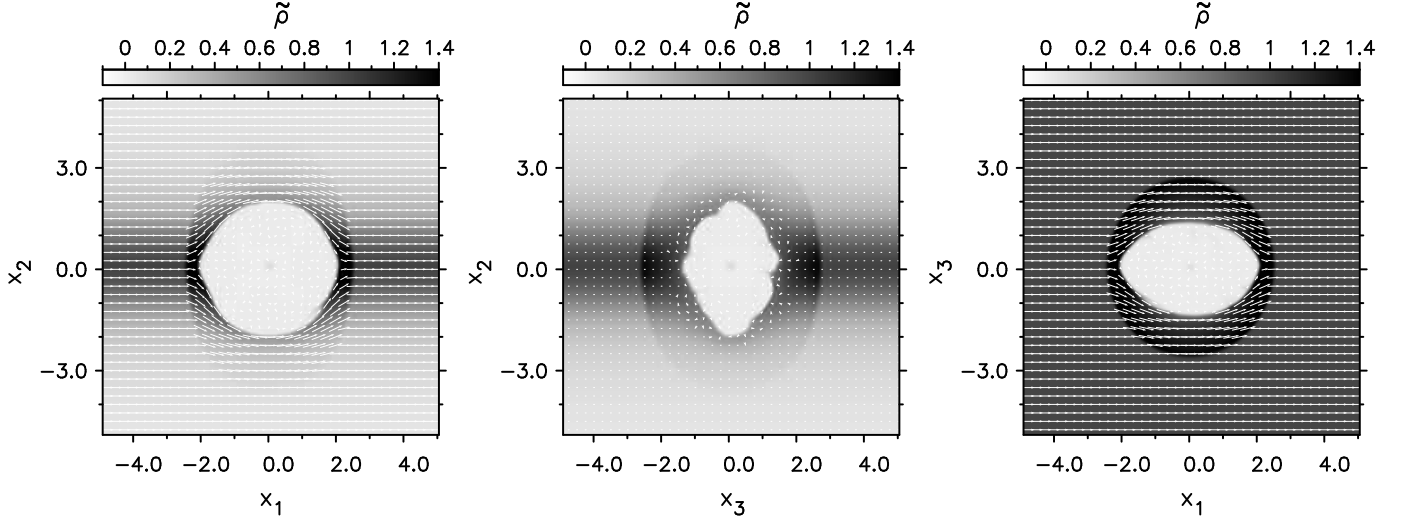


FIG. 7.— Simulation DLCBc at an age of 10 Myr. Panels show slices through the cube at the location of the source, $(x_1, x_2, x_3) = (0, 0, 0)$, in three orthogonal planes. Grayscales show the gas density on a linear scale from -0.2 (white) to 1.4 (black) cm^{-3} . The vector field depicts the projection of magnetic field vectors on the plane of the image. The unit of length on the axes is 100 pc.

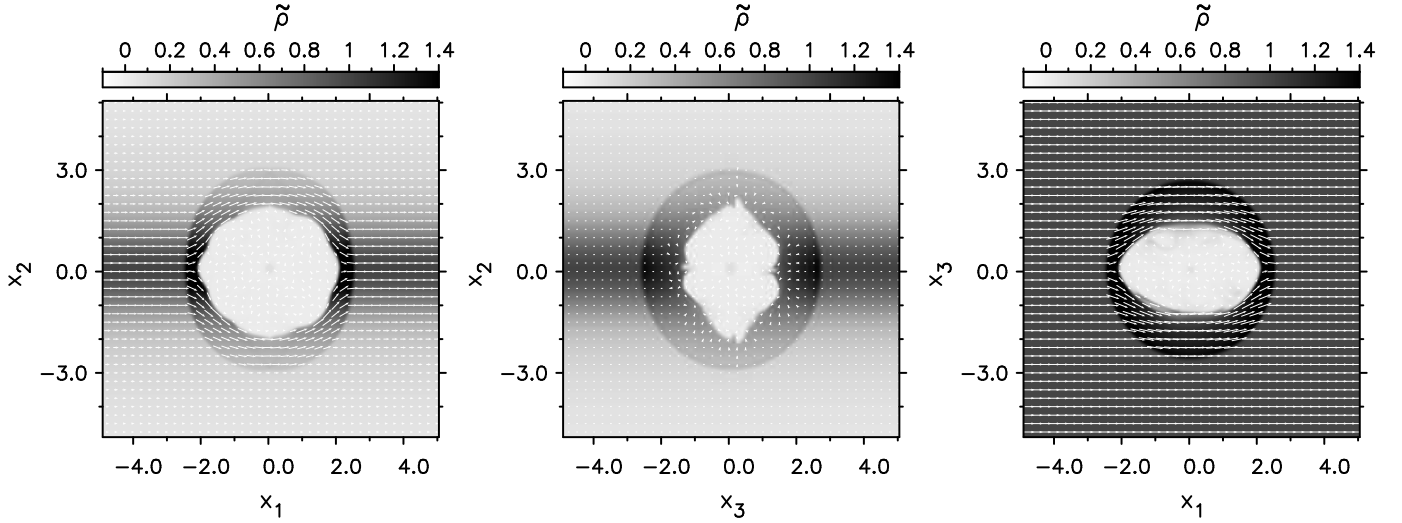


FIG. 8.— Same as Figure 7 but for Simulation DLEBc at an age of 10 Myr.

ular to the magnetic field is only 60% of its size along the magnetic field. Variation of β by a factor of three either way changes the predicted shape of the bubble in the Galactic plane from an axial ratio ~ 0.4 to ~ 0.8 at 12.5 Myr.

Figure 12 shows the time evolution of the x_2/x_1 axial ratio of the low density cavity for ExpH (diamonds), ExpCBc (stars), ExpEBc (filled squares), and the Kompaneets model (dashed line). At early times, $t \lesssim 5$ Myr, the evolution of ExpH follows the Kompaneets model. The difference between the ExpH simulation and the Kompaneets model at later times is the result of inertia of the swept-up interstellar medium. ExpCBc and ExpEBc evolve in a $\beta = 1$ medium which resists expansion along the x_2 axis. Contrary to ExpH, at early times, the axial ratios of ExpCBc and ExpEBc decrease, indicating that the expansion along the x_1 axis is faster than along the x_2 axis. This trend continues for the ExpCBc simulation while it reverses for the ExpEBc simulation where the top of the bubble accelerates at later times. In the

ExpEB simulation, confinement in the x_2 direction by the magnetic field decreases rapidly as the bubble grows beyond approximately one scale height for all values of β . This allows the top of the bubble to accelerate at later times, eventually leading to blow-out if the source is sufficiently strong (Tomisaka 1998). Breakout in our ExpEBc simulation occurs at $t \gtrsim 17.5$ Myr. The constant magnetic field in all the ExpCB simulations confines the bubble in the x_2 direction, preventing blow-out.

Taking into account differences in density and luminosity of the source, our axial ratios agree fairly well with those of Tomisaka & Ikeuchi (1986), while the results of Mac Low et al. (1989) agree better with the Kompaneets solution. Differences between our results and those of Mac Low et al. (1989) appear to be related to differences in source luminosity and the density distribution in the atmosphere.

Figure 13 shows the time evolution of the x_2/x_1 axial ratio of the low density cavity for DLH (diamonds), DLCBc (stars), and DLEBc (filled squares). The evolution

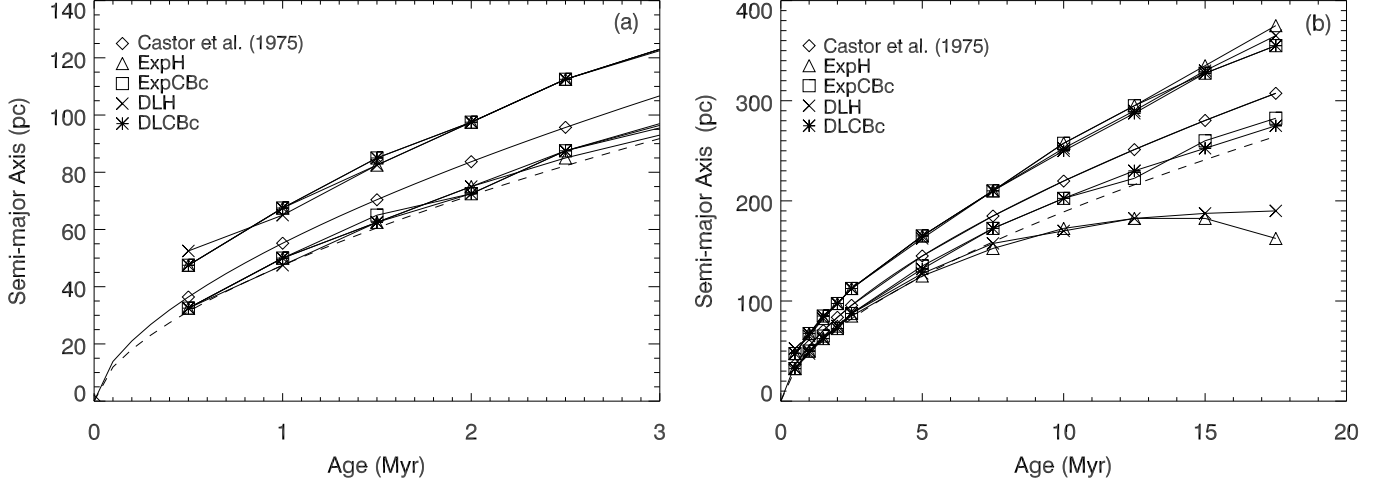


FIG. 9.— Comparison of the semi-major axis in the x_1x_3 plane of the outer shock and contact discontinuity, for a representative set of simulations, to the Castor et al. (1975) model. The semi-major axis is defined as half the diameter in the x_1 direction at the level of the source. Diamonds give the radius of the outer shock in the Castor et al. (1975) model, where the contact discontinuity is located at 86% of the radius of the outer shock (indicated by the dashed curve). (a): Enlargement of the evolution at early times. (b): Evolution at later times.

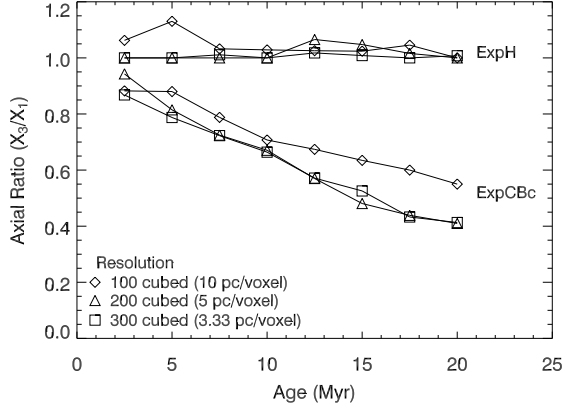


FIG. 10.— Axial ratios (x_3/x_1) of simulated bubbles as a function of time for different resolutions indicating convergence at 200×200 zones.

of the x_2/x_1 ratio of DLH shows the bubble accelerating in the x_2 direction. The axial ratio at any time is larger than those measured for ExpH because the bubble is expanding in both the positive and negative x_2 directions. DLCBc and DLEBc evolve in a $\beta = 1$ magnetic field. The shape of the cavity in the x_1x_2 plane remains nearly circular for both magnetic field configurations, even at later times. A stronger magnetic field ($\beta < 1$) results in a cavity elongated along the x_1 -axis. As for the exponential atmosphere, the bubble in the DLEB simulations eventually breaks out, whereas the bubbles in the DLCB simulations remain confined by the magnetic field.

4.4.2. Deriving Scale Height and Age From Analytic Models

The elongation of a bubble along the magnetic field has important consequences for age estimates of the bubble from observations, which usually assume axial symmetry or even spherical symmetry. The axial ratio x_3/x_1 can be observed for superbubbles in face-on galaxies, but not for Galactic superbubbles which are observed from within the Galactic plane (x_1x_3 plane). Within the Galactic plane, the available observations are the radius of the

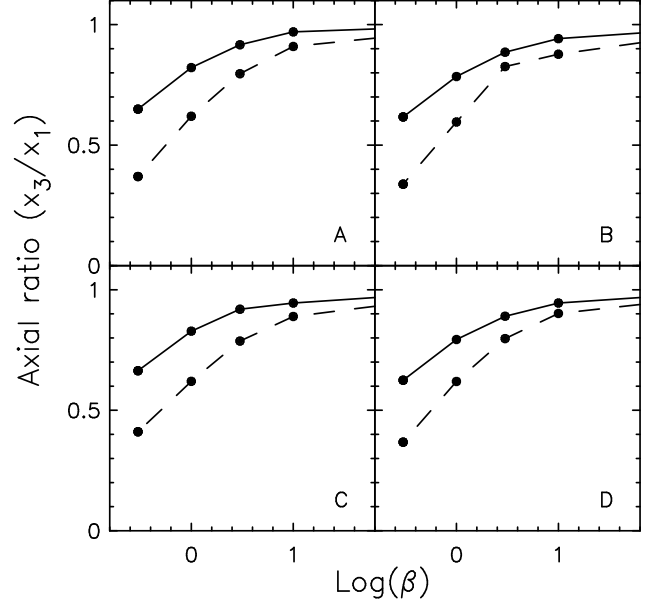


FIG. 11.— Axial ratios (x_3/x_1) of simulated bubbles as a function of β at an age of 5 Myr (solid curve) and 12.5 Myr (dashed curve). In each panel dots represent the axial ratio measured in our simulations. The curves in all four panels converge to an axial ratio of unity in the limit $\beta \rightarrow \infty$ (the hydrodynamic case). (A) Exponential atmosphere with constant magnetic field (Simulations ExpCBa-d), (B) Exponential atmosphere with constant β (ExpEBa-d), (C) Dickey and Lockman atmosphere with constant magnetic field (DLCBa-d), (D) Dickey and Lockman atmosphere with constant β (DLEBa-d). The axial ratio at the beginning of the simulations is unity for each β .

bubble in the plane of the sky and the expansion velocity perpendicular along the line of sight. The age of the bubble derived from observations is $t_{obs} = \alpha R_{obs}/v_{exp}$, assuming an expansion law of the form $R \sim t^\alpha$. The elongated shape of the bubble along the direction of the magnetic field implies that, on average, the expansion velocity is larger along the x_1 -axis than along the x_3 axis. An observer who looks at the bubble along the x_1 axis (looking along the magnetic field lines) will see the small

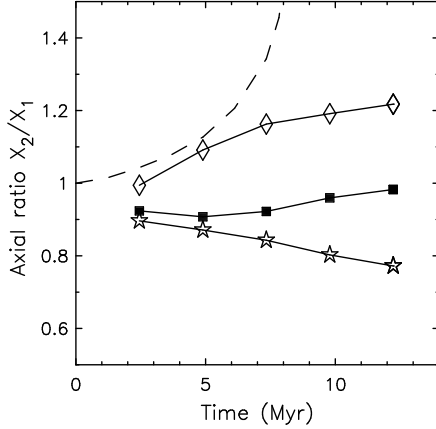


FIG. 12.— Axial ratio x_2/x_1 as a function of time for a bubble in an exponential atmosphere with $\beta = \infty$ (diamonds; ExpH), $\beta = 1$ with $B \sim \rho^{1/2}$ (filled squares; ExpEBc), and $\beta = 1$ with constant B (stars; ExpCBc). Also shown is the axial ratio of the K60 model as a function of time (dashed curve).

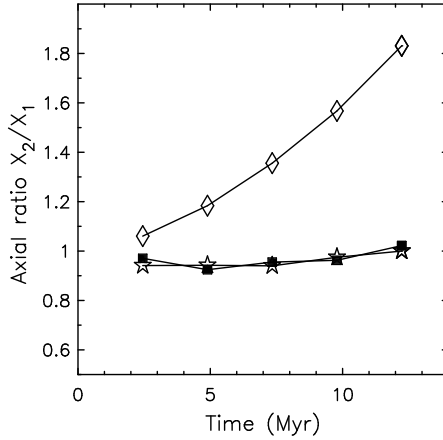


FIG. 13.— Axial ratios x_2/x_1 as a function of time for a bubble in the Dickey and Lockman atmosphere with $\beta = \infty$ (diamonds; run DLH), $\beta = 1$ with $B \sim \rho^{1/2}$ (filled squares; run DLEBc), and $\beta = 1$ with constant B (stars; run DLCBc).

dimension of the bubble along the x_3 axis but measure the larger expansion velocity along the x_1 axis. An observer who looks at the bubble along the x_3 axis (looking perpendicular to the magnetic field lines) will see the large dimension of the bubble along the x_1 axis but measure the smaller expansion velocity along the x_3 axis. The two observers will derive significantly different ages for the bubble from their observations. If the radius of the bubble along the x_1 axis is R_0 and the axial ratio x_3/x_1 is q , the age derived by observer A (looking along the field lines) is

$$t_A = \alpha \frac{qR_0}{v_{exp,A}}, \quad (22)$$

and the age derived by observer B (looking perpendicular to the field lines) is

$$t_B = \alpha \frac{R_0}{v_{exp,B}}. \quad (23)$$

On average, $v_{exp,B} = qv_{exp,A}$, therefore the ratio of the

ages derived by the two observers is

$$\frac{t_A}{t_B} = q^2. \quad (24)$$

For a moderate x_3/x_1 axial ratio of 0.8 (Figure 11), the ratio $t_A/t_B = 0.64$. Age estimates for observer A looking along the x_1 axis, and observer B looking along the x_3 axis were derived from our simulations. The ratio of these age estimates is even somewhat smaller than q^2 , especially for lower values of β , because the expansion of the shell actually stalls in the x_3 direction after a finite amount of time. This illustrates the importance of MHD effects on the derivation of the age of a superbubble.

TABLE 5
FITTING THE KOMPANEETS MODEL TO SIMULATIONS
IN THE x_3x_2 PLANE AT $t = 7.3$ MYR

\tilde{y}	H (pc)			Age (Myr)		
	ExpH	ExpCBc	ExpEBc	ExpH	ExpCBc	ExpEBc
1.4	106	78	...	5.39	3.23	...
1.5	95	70	...	5.06	3.04	...
1.6	85	62	69	4.71	2.79	3.33
1.7	75	55	61	4.26	2.54	3.02
1.8	53	2.65

The three-dimensional structure of a magnetized bubble not only affects age estimates, but also estimates of the scale height of the surrounding medium from the observed shape of the bubble. Basu et al. (1999) outline a method for fitting the Kompaneets model to observations to obtain the scale height of the ambient medium and the age of a bubble. Our simulations can be used to assess systematic errors introduced by applying an axially symmetric hydrodynamic model to a magnetized superbubble. Inspection of Figures 4, 5, 7, and 8 shows that in our simulations the Kompaneets model can only fit the shape of the cavity in an exponential atmosphere looking approximately along the magnetic field lines, or the circular shape of the cavity in a DL atmosphere looking approximately perpendicular to the field lines. In the latter case, fitting the Kompaneets model to the circular shape of the cavity would imply a very large scale height. Here we focus on fitting the Kompaneets model to the ExpH, ExpCBc, and ExpEBc simulations, in the x_3x_2 plane.

To determine a range of Kompaneets solutions that fit these bubbles, an initial estimate for \tilde{y} (Equation 4) was derived from the x_3/x_2 axial ratio of the simulation. Starting with this estimate, overlays of the Kompaneets solution were visually fitted to the simulations to obtain a range of acceptable \tilde{y} values, with the additional constraint that the source of the Kompaneets model must coincide with the source in the simulations to within 2 pixels, i.e. the radius of the source in the simulations.

Fits of the Kompaneets model have also been used to estimate the age of a bubble, if the mechanical luminosity of the source and ambient density are known. Basu et al. (1999) showed that at the level of the source, the radius of the Kompaneets bubble is nearly equal to the radius

of a spherical bubble described by Castor et al. (1975). From Equation (3), at $z = 0$, we find

$$R(z = 0, \tilde{y}) = 2H \arccos\left(1 - \frac{\tilde{y}^2}{8}\right). \quad (25)$$

As \tilde{y} and H are determined from the fit, Equation (25) can be substituted into Equation (1) with $L_s = 3 \times 10^{37}$ erg s $^{-1}$ and $\rho = 1.67 \times 10^{-24}$ g cm $^{-3}$ to find the age of the bubble.

Table 5 shows results of visual fits of the Kompaneets model to the ExpH, ExpCBc, and ExpEBc simulations at an age of 7.3 Myr, looking along the x_1 axis. Scale height and age are listed as a function of \tilde{y} for those models that provided an acceptable fit. For all three simulations, the fitted scale height is smaller for larger values of \tilde{y} , simply indicating a range of acceptable axial ratios that fit the shape of the bubble. Simulations ExpH and ExpCBc are fitted by the same range of \tilde{y} while ExpEBc is better fitted by higher values of \tilde{y} . This reflects the more elongated shape of the cavity in ExpEBc seen in Figure 5. For ExpH, we find that the scale height is close to 100 pc. Although ExpH and ExpCBc are fitted by the same range of \tilde{y} , the scale height derived from fitting ExpCBc is smaller because the bubble is more confined. This confinement of the bubble by the magnetic field while maintaining an elongated shape of the cavity is the root cause of the 30% to 50% lower scale heights resulting from fits of the Kompaneets model to a magnetized bubble. Ages derived from fits to the magnetic simulations are consistently a factor ~ 2 smaller than the actual age of the simulation. We note in passing that Koo & McKee (1990) found that the Kompaneets model blows out a factor ~ 2 earlier than their numerical hydrodynamic solutions.

As discussed earlier, the bottom of the bubble in the K60 model does not penetrate deeper than 1.4 exponential scale heights below the level of the source. If a bubble would penetrate deeper into the atmosphere, an observer could conclude that the Kompaneets model is not applicable. However, none of our simulations penetrate as deep as the limiting value of 1.4 scale heights below the level of the source. In practise, this would not constitute a conclusive test whether or not the Kompaneets model can be applied.

5. APPLICATION TO THE W4 SUPERBUBBLE

As a specific application of our simulations we investigated the result of Basu et al. (1999) that the scale height of the interstellar medium around the W4 superbubble (Normandeau et al. 1996) is as small as 25 pc, approximately a factor 4 smaller than the canonical value of 100 pc. Komljenovic et al. (1999) investigated this issue with two-dimensional MHD simulations, and suggested that the elongated shape of the bubble could only be generated by a magnetic field perpendicular to the Galactic plane (see also West et al. 2007). Our simulations allow us to consider the elongated shape of the bubble seen by an observer looking along the magnetic field lines. This perspective is not possible in two-dimensional simulations. This section is organized as follows. First we review some basic properties of the W4 region, because we found that the ambient density is a factor ~ 2.5 lower than adopted by previous authors. Second, we proceed with our analysis of the scale height near W4.

Normandeau et al. (1996) showed that an expanding shell in the Perseus arm associated with the Cas OB6 association (Braunsfurth 1983) is a conical cavity with no apparent upper boundary in HI. This structure was interpreted as a “chimney”, a large stellar wind bubble which has broken out of the Galactic disk and expands into the Galactic halo. Evidence for a vertical flow inside the cavity comes from elongated HI structures associated with a molecular cloud (Normandeau et al. 1996), and a comet-shaped molecular cloud (Normandeau et al. 1996; Heyer et al. 1996). The lower part of the bubble wall is bright in H α and is also seen in radio continuum images (Normandeau et al. 1996). The bright HII region at the bottom of the cavity is known as W4 (Westerhout 1958). The bubble appears to be confined at the bottom by a dense cloud.

The probable source of the bubble is the star cluster OCL 352 (IC 1805), which is located near the bottom of the chimney. Normandeau et al. (1996) list 9 O stars in the cluster, with the earliest spectral type O4I for the star BD+60504. The presence of the O4 star in OCL 352 makes it likely that no supernova explosion has yet occurred in the cluster, so that the bubble is a true stellar wind bubble. Most recent age determinations for the cluster are in the range 1 to 3 Myr (Hillwig et al. 2006; Rauw & De Becker 2004; Massey et al. 1995), but ages up to 5 Myr have been suggested (Kharchenko et al. 2005). The kinetic energy released in the stellar wind of the stars in the cluster is $L_{mech} = 3 \times 10^{37}$ ergs $^{-1}$ (Normandeau et al. 1996), most of which is emitted by BD+60504 and two O5 stars.

Dennison et al. (1997) reported an elongated H α shell surrounding the HI cavity that appears closed 6 $^\circ$ (230 pc) above the star cluster, outside the field of view of the original HI images of Normandeau et al. (1996). Extended HI images that cover the top of the H α shell do not show a cap in the neutral gas (Normandeau 2000). The H α shell was interpreted as the inner wall of the superbubble ionized by the stars in OCL 352. Dennison et al. (1997) found that the age of the superbubble exceeds the maximum possible age of OCL 352 by a factor ~ 3 , using the mechanical luminosity of the star cluster ($L_{mech} = 3 \times 10^{37}$ ergs $^{-1}$) and the density of the ambient medium ($n_0 = 5$ cm $^{-3}$) given by Normandeau et al. (1996). The large dynamical age of the bubble was taken as an indication that the star cluster OCL 352 by itself may not be the only source of the superbubble. Basu et al. (1999) found that the age of the bubble is consistent with the age of the star cluster by applying the K60 model to the W4 superbubble, assuming a scale height of only 25 pc for the ambient medium. However, Dennison et al. (1997) noted that a lower ambient density could decrease the dynamical age derived for the W4 superbubble.

The original HI number density was derived by Normandeau et al. (1996) from an HI column density map. This map was obtained by integration of the HI brightness temperature over a velocity range of 14.8 km s $^{-1}$. The ambient density was then calculated by dividing the HI column density adjacent to the cavity by the diameter of the bubble, assuming that all the HI emission is local to the W4 superbubble. This assumption leads to a significant over-estimate of the ambient

density, because HI emission in the velocity range of the bubble originates from a much longer section of the line of sight. We re-analyzed the HI data of the W4 region, now publicly available as part of the Canadian Galactic Plane Survey (Taylor et al. 2003), to re-determine the ambient density.

The HI column density inside the cavity of the W4 superbubble, avoiding the HI features known to be inside the cavity (Normandeau et al. 1996), is $1.1 \times 10^{21} \text{ cm}^{-2}$. The medium inside the superbubble is expected to be a highly ionized tenuous plasma at a temperature of a few million Kelvin. The ionized bubble wall seen on both sides of the cavity in radio continuum and H α emission shows that the interior of the bubble is optically thin to Lyman continuum photons. Dennison et al. (1997) and Basu et al. (1999) assume this to be true in their analysis of the ionization of the bubble wall by the star cluster. Therefore, HI observed inside the cavity must be located in the foreground and the background. Some of this HI emission could in principle belong to the bubble wall if the expansion of the superbubble had stalled. There is no reason to believe that the expansion of the bubble has stalled because the source is still active.

Although the evidence that the HI steamers identified by Normandeau et al. (1996) are located inside the cavity of the W4 bubble is compelling, the HI emission that seems to partly fill the cavity everywhere is likely unrelated gas, that was included in the density estimate of Normandeau et al. (1996). If the HI column density inside the cavity is subtracted, the density of the ambient medium is reduced to $\sim 2 \text{ cm}^{-3}$ assuming the same line-of-sight dimension of the bubble. A better estimate of the density of the ambient medium is obtained by dividing the mass of the shell of swept-up gas by the volume of the cavity. This is impractical for the W4 bubble because there is no clear limb-brightened HI shell visible in the column density map. Basu et al. (1999) found a higher density of 10 cm^{-3} from their analysis of the shape of the ionization front, which depends on the details of their model. Although the lower value of the ambient density derived from the HI data may not resolve the age problem altogether, we follow the suggestion by Dennison et al. (1997) that the location of the cluster is strong evidence for its identification as the source of the superbubble.

We now return to the issue of the small scale height found by Basu et al. (1999). Normandeau (2000) found no evidence for such a small scale height in HI images of the region, but, as noted before, the HI images are contaminated to some extent by emission in the foreground and background. The presence of molecular gas with a small scale height may have contributed to the result obtained by Basu et al. (1999), but the molecular gas traced by the CO line appears too fragmented to confine the shape of the bubble. The scale height found by fitting the Kompaneets model to the observed shape of the bubble may also be artificially small by a factor 2 (see §4.4.2) for an observer looking along the magnetic field parallel to the Galactic plane. This factor is not enough to explain the very small scale height derived by Basu et al. (1999). Also, the age derived by Basu et al. (1999) would be too small by a factor 2, further increasing the discrepancy between the dynamical age of the

bubble and the age of the star cluster. None of our simulations evolve into a cavity that is as narrow as the W4 super bubble.

6. FARADAY ROTATION BY A MAGNETIZED BUBBLE

Polarimetric observations of the Galactic plane at arcminute resolution (Taylor et al. 2003; McClure-Griffiths et al. 2005) allow measurements of Faraday rotation of diffuse Galactic synchrotron radiation and background compact extragalactic sources to probe the magneto-ionic interstellar medium down to parsec scales. The plane of polarization of linearly polarized synchrotron emission rotates by an angle $\Delta\theta$ (radians) as the radiation passes through a magnetized plasma according to $\Delta\theta = \lambda^2 RM$, with λ the wavelength of the radiation in meters. The line-of-sight integral

$$RM = 0.812 \int n_e \mathbf{B} \cdot d\mathbf{l} \quad (26)$$

is the rotation measure (radians m^{-2}), with n_e the electron density (cm^{-3}), and $\mathbf{B} \cdot d\mathbf{l}$ the magnetic field vector B (μG) projected onto the line of sight (in parsec). The rotation measure can be determined observationally by observing $\Delta\theta$ at different, but closely spaced wavelengths. Structure along the line of sight may create a measurable rotation of the plane of polarization, but it may not have a sufficiently large emission measure for any thermal emission to be detected.

Equation (26) cannot be inverted to obtain a unique solution to the magnetic field structure, even if independent information on the electron density n_e along the line of sight is available. Instead, the data can be interpreted by line-of-sight integration of a model distribution of the density and magnetic field, which depends critically on the assumed distributions of the electron density and magnetic field. If an ad hoc model for density and magnetic field is adopted to interpret the observations, careful consideration should be given to basic questions regarding self-consistency, uniqueness and dynamical properties of the proposed model. Our three-dimensional MHD simulations of magnetized superbubbles constitute a significant step forward in the modeling of Faraday rotation by Galactic superbubbles. In this paper, we only consider the bubble as a Faraday screen that does not emit synchrotron emission. This situation applies in particular to compact polarized sources in the background.

The simulations provide a self-consistent set of models that can be used to calculate the rotation measure imposed on background emission by a magnetized superbubble. The non-spherical evolution of the superbubble described in Section 4 may have very significant effects on the predicted rotation measure. The effect of nearby superbubbles on Faraday rotation of background sources was first discussed by Vallée (1993). In this paper we discuss only the Faraday rotation signature of distant bubbles, for which we can assume that all lines of sight are parallel. We assume here that the bubble is completely ionized. This allows a first exploration of the general effects of the topology of the density and magnetic field, without introducing more parameters.

Figure 14 shows the rotation measure for a line of sight along the x_3 axis (looking perpendicular to the Galactic

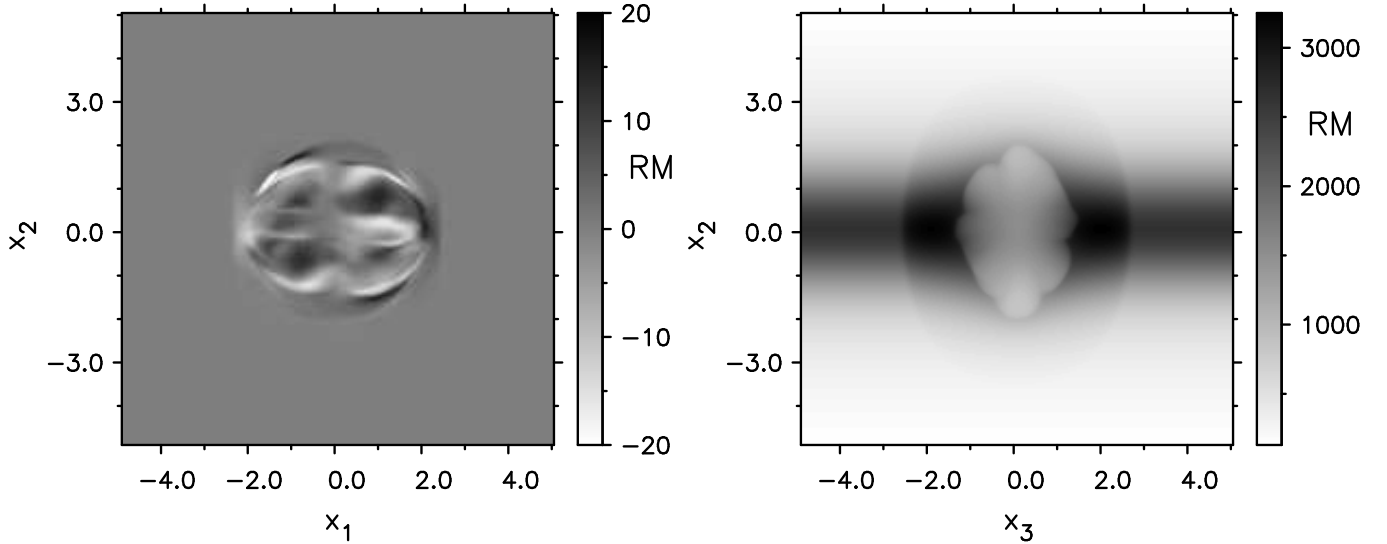


FIG. 14.— Images of rotation measure of the simulation DLCBc at age 10 Myr (see also Figure 7) along a direction perpendicular to the undisturbed Galactic magnetic field (left) and along the direction of the magnetic field (right). Grayscales are linear from -20 to $+20$ radians m^{-2} (left) and from 130 to 3252 radians m^{-2} (right). Wrapping of the magnetic field lines around the low-density cavity creates significantly different Faraday rotation signatures for the same bubble seen from different directions. If the line of sight is perpendicular to the Galactic magnetic field, the shell of swept-up interstellar medium is almost invisible in the rotation measure map. If the line of sight is along the Galactic magnetic field, the largest rotation measures are associated with the (thick) shell. The unit of length on the axes is 100 pc.

magnetic field) and the x_1 axis (looking along the Galactic magnetic field) of the simulation DLCBc (Table 3) at an age of 10 Myr (Figure 7). The line-of-sight integration of Equation (26) was done through the entire simulated volume as shown in Figure 7. It includes some undisturbed medium in the foreground and the background of the bubble.

Comparing the rotation measure maps with the density and magnetic field structure (Figure 7) reveals some general characteristics of the Faraday rotation of all bubbles in our simulations. As the magnetic field is pushed aside, the field lines wrap around the expanding cavity. The largest amplification and the largest change of direction of the magnetic field occur just outside the cavity, in the equatorial plane (for the DL density distribution). The density is also enhanced, compared with the surrounding undisturbed interstellar medium, but by different amounts depending on location in the shell. Simulations with a small scale height of the Galactic magnetic field ($B \sim \rho^{1/2}$) show this compression also at the top of the bubble, whereas simulations with a large scale height of the magnetic field (constant B) do not. The largest Faraday rotation therefore occurs in a relatively thin region around the cavity, being strongest close to the Galactic plane (see Figure 14). The Faraday rotation inside the cavity is much smaller by comparison, because of the low density and the low chaotic magnetic field there.

If the line of sight is perpendicular to the direction of the undisturbed magnetic field, the near and the far side of the bubble wall have rotation measures up to ~ 100 radians m^{-2} , with opposite signs. These mostly cancel each other, but asymmetries between the front side and the back side of the shell create structure in the rotation measure distribution. Asymmetries arise from the instabilities in the shell mentioned in Sections 4.2.2 & 4.4. The strongest signal is expected from asymmetries that occur in locations where a perfectly symmetric bubble would

have bent the Galactic magnetic field sufficiently to create a significant line of sight component of the magnetic field. As the magnetic field is tightly wrapped around the cavity, the highest values of the rotation measure resulting from front-to-back asymmetries are therefore expected for lines of sight that intersect the cavity, away from the vertical axis that intersects the source. Our three-dimensional simulations contain such asymmetries, resulting in the structures seen in Figure 14 with amplitudes of the order of 20 radians m^{-2} .

If the line of sight is parallel to the direction of the undisturbed magnetic field, rotation measures are much higher everywhere than in the previous case. The front and back side of the shell reinforce each other, and high rotation measures are expected for lines of sight that intersect the shell. The top of the bubble increases the rotation measure a few hundred parsecs above the Galactic plane by $\sim 20\%$ compared with the undisturbed atmosphere in Figure 14. For the simulation DLEBc (small magnetic scale height), the increase is $\sim 30\%$ compared with the undisturbed atmosphere. Within 100 pc from the Galactic plane, the rotation measure varies with location because of the bubble, but the mean of the rotation measure across the bubble is almost the same as the mean rotation measure of the undisturbed atmosphere. Here, the effect of the bubble is to create a significant variation in rotation measure for different lines of sight, with little effect on the mean rotation measure taken over a large area. Super bubble shells may therefore enhance the rotation measure in the disk-halo interface and affect estimates of the scale height of the Galactic magnetic field from rotation measure analysis.

Vallée & Bignell (1983) reported a large magnetized bubble associated with the Gum nebula, based on a number of high rotation measures towards extragalactic sources. Recently, Stil & Taylor (2007) found this bubble in an all-sky image of depolarization of extragalactic

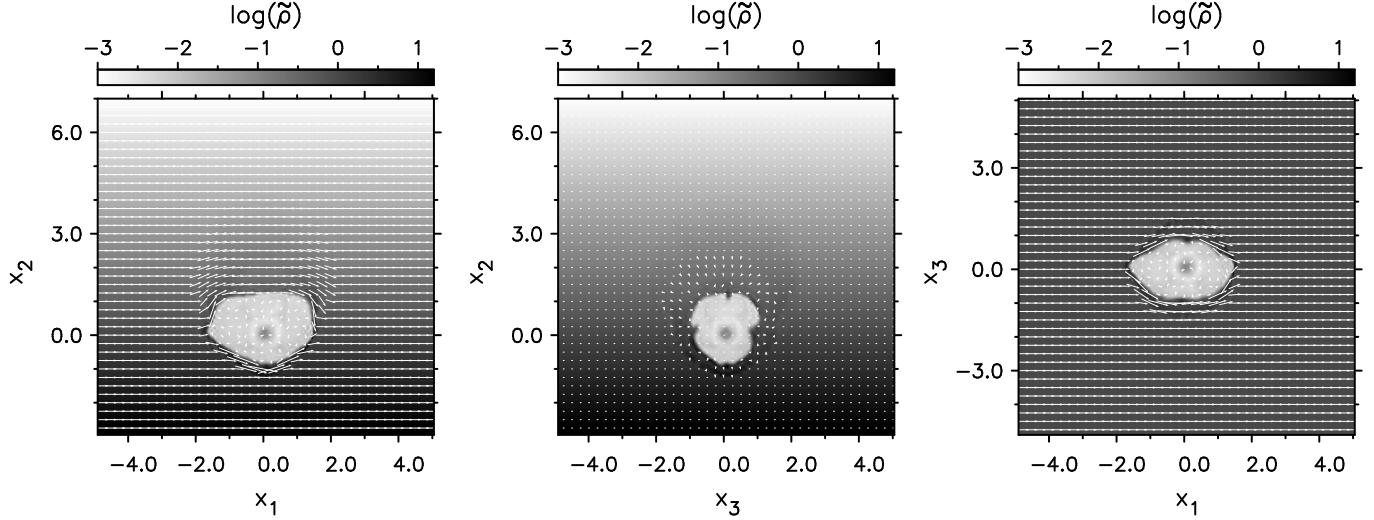


FIG. 15.— Simulation ExpCB with cooling at an age of 10 Myr for comparison with Figure 4. Magnetic field initially oriented along x_1 axis, $\beta = 1$. Panels show slices through the cube at the location of the source, $(x_1, x_2, x_3) = (0, 0, 0)$, in three orthogonal planes. Grayscales show the gas density on a logarithmic scale from 10^{-3} (white) to $10^{1.2}$ (black) cm^{-3} . The vector field depicts the projection of magnetic field vectors on the plane of the image. The unit of length on the axes is 100 pc.

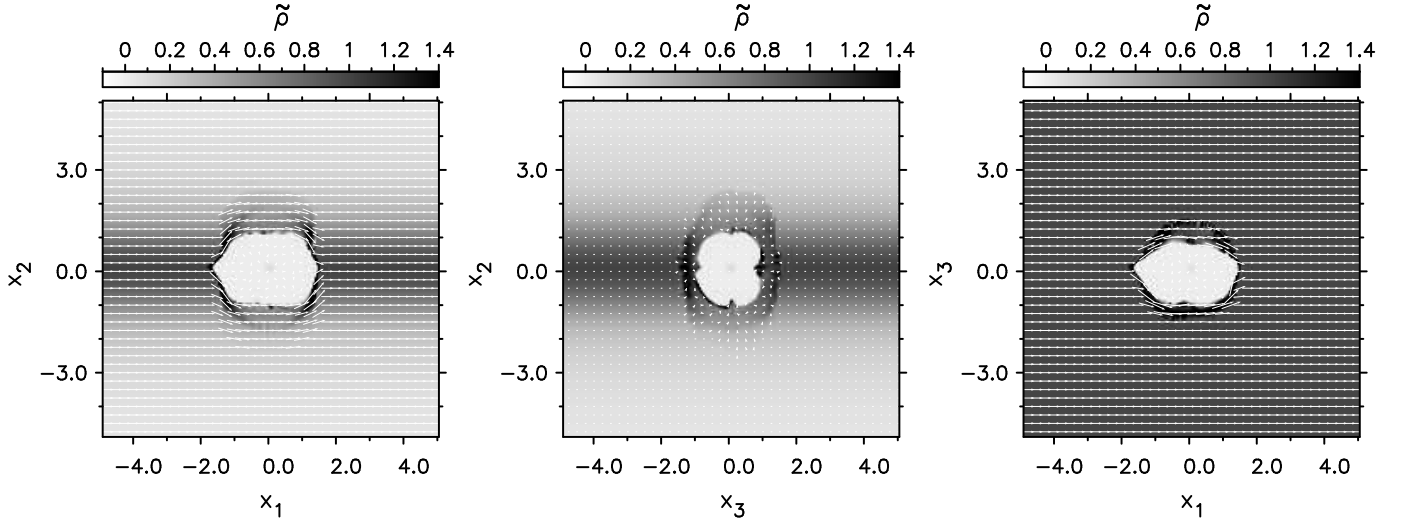


FIG. 16.— Simulation DLCB with cooling at an age of 10 Myr for comparison with Figure 7. Magnetic field initially oriented along x_1 axis, $\beta = 1$. Panels show slices through the cube at the location of the source, $(x_1, x_2, x_3) = (0, 0, 0)$, in three orthogonal planes. Grayscales show the gas density on a logarithmic scale from 10^{-3} (white) to $10^{1.2}$ (black) cm^{-3} . The vector field depicts the projection of magnetic field vectors on the plane of the image. The unit of length on the axes is 100 pc.

sources, that was associated with excess rotation measure. This bubble stands out in the data because of the high rotation measure in the shell. The line of sight in this case is nearly parallel to the magnetic field in the local spiral arm.

7. THE EFFECTS OF COOLING

So far we have discussed adiabatic simulations of super bubbles as an approximation that energy losses are compensated by an internal or an external radiation field. In this section we briefly discuss simulations with cooling in the two main density stratifications discussed in this paper: the exponential atmosphere and the Dickey & Lockman atmosphere. The cooling represents an extra term in the energy equation (10) and is implemented as an explicit source term in the code. As with all physical processes, there is a maximum allowed time step for nu-

merical stability associated with the cooling; in our case it is reset to 10% of the radiative cooling time when it is below the normal hydrodynamic CFL condition.

The cooling function by Raymond et al. (1976) and Dalgarno & McCray (1972), using the abundances of Allen (1973), was implemented into zeus-mp in the form of analytic expressions adopted by Tomisaka et al. (1981). Although some abundances were revised downwards later, the difference between the cooling rates adopted in our simulations and the solar abundance cooling curve of Gnat & Sternberg (2007) is smaller than other sources of uncertainty introduced by finite resolution, and ionization by the central star cluster. If an accuracy better than a factor ~ 3 is required in the cooling rate, the location of the superbubble in the Galaxy also becomes important because of variation in the abundances with location in the Galaxy (e.g. Rudolph et al.

2006).

The radiatively cooled simulations were done in atmospheres maintained at a temperature of 8000 K, with the same resolution as the adiabatic simulations discussed in Section 4, and with the same mechanical luminosity of the source. In these simulations, cooling begins at a time $t = 4$ Myr, soon after the first supernova explosion, at the beginning of the radiative phase following MacCray & Kafatos (1987). The effects of cooling on the shape of the cavity are evaluated at $t = 10$ Myr.

7.1. Results with cooling

Figure 15 and Figure 16 show simulations of a bubble with cooling in an exponential atmosphere and in a Dickey & Lockman atmosphere at an age of 10 Myr. These figures can be compared with the adiabatic simulations shown in Figure 4 and Figure 7. Qualitatively the features in these simulations are very similar. The cavity is elongated along the direction of the magnetic field. The shell is thicker in directions perpendicular to the magnetic field in the undisturbed atmosphere (x_2 and x_3), while significant compression of the swept-up material in the direction of the magnetic field leads to a thinner, denser shell. Closer inspection shows that the cavities of both cooled simulations are more elongated in the direction of the magnetic field (x_1). The shell also seems to display stronger instabilities, leading to irregularities in the shape of the cavity, and increased scatter in the derived axial ratios of the cavity. As expected, the simulations with cooling lead to shells that are thinner, with a higher density and stronger magnetic field, than the adiabatic simulations. The effect of resolution on the cooled regions is to smear out small-scale high-density structure with the shortest cooling time and the lowest temperature. De Avillez & Breitschwerdt (2004) found convergence in the maximum density and lowest temperature in their simulations for a grid size $\lesssim 1.1$ pc. The density and temperature inside the swept-up shell in our simulations are probably also affected by resolution, but this paper focuses on the shape of the bubble, not the conditions inside the shell. García-Segura & López (2000) found that the shape of planetary nebulae in their simulations was not affected by resolution.

Figure 17 shows the evolution of the axial ratios as a function of time in these simulations. We find that the axial ratio x_2/x_1 of a bubble in the Dickey & Lockman atmosphere is most affected by cooling (compare Figure 17a with Figures 12 and 13). In the adiabatic simulation, the cavity remains nearly circular to an age of 10 Myr, while in the cooled simulation the cavity is more elongated in the direction of the magnetic field. Note the change in evolution of the x_2/x_1 axial ratio just after the onset of cooling. The effect of cooling on the axial ratio x_2/x_1 compared with the adiabatic case is less strong for the exponential atmosphere, but here too the cavity becomes more elongated in the direction of the magnetic field. A stronger elongation is also seen in the x_3/x_1 axial ratio (compare Figure 17b with Figure 10), but the effect is smaller than on the axial ratio x_2/x_1 .

The observed change in axial ratios in the presence of cooling is most likely the result of increased magnetic tension exerted by the stronger magnetic field in the dense shell that surrounds the cavity. This restricts the expansion perpendicular to the field (x_2 and x_3) more

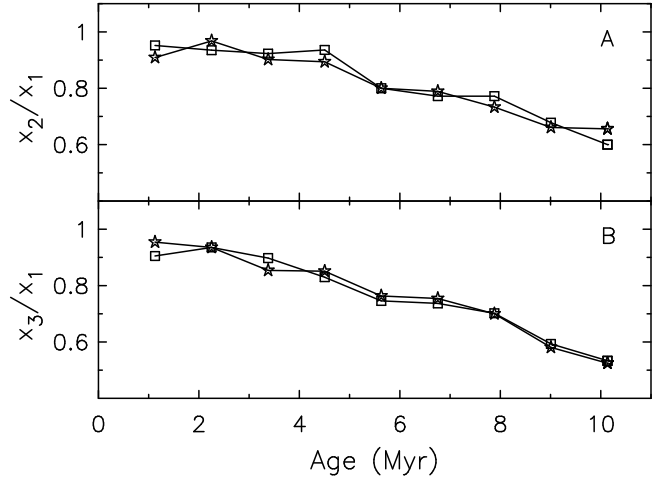


FIG. 17.— Axial ratio x_2/x_1 (A) and x_3/x_1 (B) as a function of the age of the bubble for cooled simulations in an exponential atmosphere (stars) and a Dickey & Lockman atmosphere (squares). Panel (A) may be compared with Figures 12 and 13, and panel B may be compared with Figure 10.

in the cooled simulations than in the adiabatic simulations. Coupling between the magnetic field and the neutral shell is maintained through a small ionized fraction in the shell, and ion-neutral collisions. A complete parameter study of simulations with cooling is beyond the scope of this paper.

At least some superbubbles have a substantial fraction of the mass of the shell ionized by the stars inside. In simulations with cooling, the cooling time of the shell is very short compared to the age of the bubble, and a dense neutral shell forms. Ideally, radiative transport of the ionizing flux of the star cluster and any unrelated massive hot stars in the simulation volume should be included in the simulations. Solving the radiative transport every time step in the simulations is a computational challenge. The mean free path of an ionizing photon is substantially smaller than the resolution of the simulations. The ionizing flux decreases rapidly with time as the most massive stars explode as a supernova after ~ 3 Myr, and the shell will eventually cool and become neutral. The implicit assumption in this paper by applying adiabatic evolution to this problem is that heating by photo-ionization is balanced by cooling. While this is a simplification, the observed ionization of superbubble walls suggests that heating by ionization of the shell is a non-negligible term in the energy equation of the shell that is not included in simulations with cooling only.

8. CONCLUSIONS

We present three-dimensional MHD simulations of a superbubble evolving in a magnetized medium. In these simulations, we assume two different atmospheric models, exponential and Dickey & Lockman (1990), and two different magnetic field configurations, constant magnetic field and constant β , for varying values of the magnetic field strength. With these simulations we aim to study the importance of MHD effects on the interpretation of observed superbubbles.

As noted before by Tomisaka (1998), a superbubble in a magnetized medium becomes significantly elongated along the magnetic field. We find that the axial ratio of the bubble in the Galactic plane is ~ 0.8 after 5 Myr and

~ 0.6 after 12.5 Myr, depending on the age of the bubble and the strength of the magnetic field but not on the vertical structure of either the magnetic field or the gas. The elongated shape of the bubble in the Galactic plane may lead to significant errors in the age determination of magnetized superbubbles from observations using symmetric hydrodynamic models. The derived age depends on the location of the observer. The ratio of the smallest age to the largest age derived by observers assuming axial or spherical symmetry is found to be proportional to the square of the axial ratio of the bubble in the Galactic plane, which creates a discrepancy in the age of up to a factor ~ 4 .

We have analyzed systematic errors in the age of the bubble and the scale height of the ambient medium introduced by fitting the Kompaneets model to a magnetized superbubble looking along the magnetic field lines. The scale height may be underestimated by 30% to 50% and the age by 50%. In particular, we investigated the curiously small scale height of the interstellar medium near the W4 superbubble found by Basu et al. (1999). We re-analyzed HI data from the Canadian Galactic Plane Survey and found that the density of the ambient medium $n_H \approx 2\text{cm}^{-3}$ which is smaller than previously thought. This lower density helps to diminish the apparent age discrepancy between the W4 bubble and the star cluster OCL 352. However, our analysis of the systematic errors introduced by fitting the Kompaneets model shows that they are not big enough to explain the scale height of 25 pc found by Basu et al. (1999) for the W4 region.

We use the MHD simulations to predict the rotation measure distribution of superbubbles based on three-dimensional MHD simulations, and emphasize the importance of such simulations to make these predictions. As expected, the appearance of a magnetized superbubble depends on the perspective of the observer. If the observer looks along the magnetic field lines, the largest rotation measures are seen at the intersection of the shell with the Galactic plane. The rotation measure is increased at larger distances from the Galactic plane. If an observer in the Galactic plane looks perpendicular to the magnetic field lines, the rotation measures are much smaller, but most importantly most of the structure in rotation measure appears in projection on the low-density cavity, and not on the shell surrounding it.

The simulations and analysis presented in this paper highlight the importance of three-dimensional MHD simulations of superbubbles evolving in the Galactic magnetic field to the interpretation of new high-resolution images of the Galactic plane at radio wavelengths from the International Galactic Plane Survey.

This research has been enabled by the use of WestGrid computing resources, which are funded in part by the Canada Foundation for Innovation, Alberta Innovation and Science, BC Advanced Education, and the participating research institutions. WestGrid equipment is provided by IBM, Hewlett Packard and SGI

APPENDIX

THE KOMPANEETS SOLUTION AT EARLY TIMES

We show that the Kompaneets solution at early times can be approximated as an expanding sphere with a center that moves upward from the location of the source. This analytic derivation explains quantitatively the behavior of the Kompaneets solution in Figure 3.

The center of the bubble along the vertical axis follows from the expressions for the top and bottom of the bubble (Equation 6)

$$z_c = \frac{z_1 + z_2}{2} = -H \ln[1 - (\tilde{y}/2)^2]. \quad (\text{A1})$$

The half-diameter of the Kompaneets solution in the vertical direction is

$$R_z = \frac{z_1 - z_2}{2} = -H \ln\left[\frac{1 - \tilde{y}/2}{1 + \tilde{y}/2}\right]. \quad (\text{A2})$$

The maximum radius R_h of the Kompaneets solution in a direction perpendicular to the density gradient was given by Bisnovatyi-Kogan & Silich (1995) and Basu et al. (1999),

$$R_h = 2H \arcsin(\tilde{y}/2). \quad (\text{A3})$$

The Taylor expansion of z_c , R_z , and R_h in $x = \tilde{y}/2$ to third order in x is

$$z_c = Hx^2 + O(x^4), \quad (\text{A4})$$

where $O(x^4)$ is the remainder that contains terms of order x^4 or higher. Similarly, we have

$$R_z = 2Hx + \frac{2}{3}Hx^3 + O(x^5), \quad (\text{A5})$$

and

$$R_h = 2Hx + \frac{1}{3}Hx^3 + O(x^5), \quad (\text{A6})$$

so the difference $R_z - R_h$ is of order x^3

$$R_z - R_h = \frac{1}{3}Hx^3 + O(x^5). \quad (\text{A7})$$

We see that for small x , the shift in the centre is Hx^2 , which is of second order in x . The difference $R_z - R_h$ is of third order in x . The Kompaneets solution for small \tilde{y} can therefore be approximated by a spherical bubble that rises in the atmosphere. The center according to equation A1 is shown in Figure 3. The offset is clear, where the Kompaneets model is still visually a circle. Although both the numerical simulation and the Kompaneets model have an axial ratio that is near unity, the difference between the Kompaneets model and the numerical simulation is in the fact that the former is not centered on the source.

REFERENCES

- Allen, C. W. 1973, *Astrophysical Quantities* 3rd ed.; London: Athlone Press
- Basu, S., Johnstone, D., & Martin, P. G. 1999, *ApJ*, 516, 843
- Bisnovatyi-Kogan, G. S., & Silich, S. A. 1995, *Reviews of Modern Physics*, 67, 661
- Braunsfurth, E. 1983, *A&A*, 117, 297
- Breitschwerdt, D. & de Avillez, M. A. 2006, *A&A*, 452, L1
- Brown, A. G. A., Hartmann, D., & Burton, W. B. 1995, *A&A*, 300, 903
- Callaway, M. B., Savage, B. D., Benjamin, R. A., Haffner, L. M., & Tufte, S. L. 2000, *ApJ*, 532, 943
- Castor, J., McCray, R., & Weaver, R. 1975, *ApJ*, 200, L107
- Colella, P., & Woodward, P. R. 1984, *Journal of Computational Physics*, 54, 174
- Dalgarno, A., & McCray, R. A. 1972, *ARA&A*, 10, 375
- de Avillez, M. A., & Breitschwerdt, D. 2004, *A&A*, 425, 899
- de Avillez, M. A., & Breitschwerdt, D. 2005, *A&A*, 436, 585
- Dennison, B., Topasna, G. A., & Simonetti, J. H. 1997, *ApJ*, 474, L31
- Dickey, J. M., & Lockman, F. J. 1990, *ARA&A*, 28, 215
- Ehlerová, S. & Palous, J. 1999, *A&A*, 350, 457
- Evans, C. R., & Hawley, J. F. 1988, *ApJ*, 332, 659
- Falle, S. A. E. G. 2002, *ApJ*, 577, L123
- Ferrière, K. M., Mac Low, M.-M., Zweibel, E. G. 1991, *ApJ*, 375, 239
- Fuchs, B., Breitschwerdt, D., de Avillez, M. A., Dettbarn, C., & Flynn, C. 2006, *MNRAS*, 373, 993
- García-Segura, G. & López, J. A. 2000, *ApJ*, 544, 336
- Gnat, O., & Sternberg, A. 2007, *ApJS*, 168, 213
- Godunov, S. K. 1959, *Matematicheskii Sbornik*, 47, 271
- Gooch, R. 1996, in *ASP Conf. Ser. 101, Astronomical Data Analysis Software and Systems V*, ed. Jacoby, G. H. & Barnes, J., 80
- Gregori, G., Miniati, F., Ryu, D., & Jones, T. W. 2000 *ApJ*, 543, 775
- Hayes, J. C., Norman, M. L., Fiedler, R. A., Bordner, J. O., Li, P. S., Clark, S. E., ud-Doula, A., & Mac Low, M.-M. 2006, *ApJS*, 165, 188
- Hawley, J. F. & Stone, J. M. 1995, *Comput. Phys. Commun.* 89, 127
- Heiles, C. 1976, *ApJ*, 208, L137
- Heiles, C. 1984, *ApJS*, 55, 585
- Heiles, C. 1998, *ApJ*, 498, 689
- Heyer, M. H., Brunt, C., Snell, R. L., Howe, J., Schloerb, F. P., Carpenter, J. M., Normandeau, M., Taylor, A. R., Dewdney, P. E., Cao, Y., Terebey, S., Beichman, C. A. 1996, *ApJ*, 464, L175
- Hillwig, T. C., Gies, D. R., Bagnuolo Jr., W. G., Huang, W., McSwain, M. V., & Wingert, D. W. 2006, *ApJ*, 639, 1069
- Kharchenko, N. V., Piskunov, A. E., Röser, S., Schilbach, E., & Scholz, R.-D. 2005, *A&A*, 438, 1163
- Koo, B.-C., & McKee, C. F. 1990, *ApJ*, 354, 513
- Komljenovic, P. T., Basu, S., & Johnstone, D. 1999, in *ASP Conf. Ser. 168, New Perspectives on the Interstellar Medium*, ed. A. R. Taylor, T. L. Landecker, & G. Joncas, (San Francisco: ASP), 299
- Kompaneets, A. S. 1960 (K60), *Soviet Phys. Dokl.*, 5, 46
- Korpi, M. J., Brandenburg, A., Shukurov, A., & Tuominen, T. 1999, *A&A*, 350, 230
- McCray, R., & Kafatos, M. 1987, *ApJ*, 317, 190
- Maciejewski, W., Murphy, E. M., Lockman, F. J., & Savage, B. D., *ApJ*, 469, 238
- Mac Low, M. M., & McCray, R. 1988, *ApJ*, 324, 776
- Mac Low, M.-M., McCray, R., & Norman, M. L. 1989, *ApJ*, 337, 141
- Massey, P., Johnson, K. E., & Degioia-Eastwood, K. 1995, *ApJ*, 454, 151
- McClure-Griffiths, N. M., Dickey, J. M., Gaensler, B. M., Green, A. J., Haverkorn, M., & Strasser, S. 2005, *ApJS*, 158, 178
- McClure-Griffiths, N. M., Dickey, J. M., Gaensler, B. M., & Green, A. J. 2003, *ApJ*, 594, 833
- McClure-Griffiths, N. M., Dickey, J. M., Gaensler, B. M., & Green, A. J. 2002, *ApJ*, 578, 176
- McKee, C. F., & Ostriker, J. P. 1977, *ApJ*, 218, 148
- Mineshige, S., Shibata, K., & Shapiro, P. R. 1993, *ApJ*, 409, 663
- Norman, M. L. 2000, *Revista Mexicana de Astronomia y Astrofisica Conference Series*, 9, 66
- Normandeau, M., Taylor, A. R., & Dewdney, P. E. 1996, *Nature*, 380, 687
- Normandeau, M. 2000, in *ASP Conf. Ser. 221, Stars, gas and dust in galaxies: exploring the links*, ed. D. Alloin, K. Olsen & G. Galaz, (San Francisco: ASP), 41
- Pidopryhora, Y., Lockman, F. J., & Shields, J. C. 2007, *ApJ*, 656, 928
- Rauw, G., & De Becker, M. 2004, *A&A*, 421, 693
- Raymond, J. C., Cox, D. P., & Smith, B. W. 1976, *ApJ*, 204, 290
- Reynolds, R. J., & Ogden, P. M. 1979, *ApJ*, 229, 942
- Reynolds, R. J., Sterling, N. C., & Haffner, L. M. 2001, *ApJ*, 558, L101
- Robinson, K., et al. 2004, *ApJ*, 601, 621
- Staff, J., Jorgensen, M., & Ouyed, R. 2004, preprint (astro-ph/0402121)
- Rudolph, A. L., Fich, M., Bell, G. R., Norsen, T., Simpson, J. P., Haas, M. R., Erickson, E. F. 2006, *ApJS*, 162, 346
- Stil, J. M., Taylor, A. R., Dickey, J. M., Kavars, D. W., Martin, P. G., Rothwell, T. A., Boothroyd, A. I., Lockman, F. J., & McClure-Griffiths, N. M. 2006, *AJ*, 132, 1158
- Stil, J. M., & Taylor, A. R. 2007, *ApJ*, 663, L21
- Stone, J. M., & Norman, M. L. 1992a, *ApJS*, 80, 753
- Stone, J. M., & Norman, M. L. 1992b, *ApJS*, 80, 791
- Taylor, A. R., Gibson, S. J., Peracaula, M., Martin, P. G., Landecker, T. L., Brunt, C. M., Dewdney, P. E., Dougherty, S. M., Gray, A. D., Higgs, L. A., Kerton, C. R., Knee, L. B. G., Kothes, R., Purton, C. R., Uyaniker, B., Wallace, B. J., Willis, A. G., & Durand, D. 2003, *AJ*, 125, 3145
- Tomisaka, K., Habe, A., & Ikeuchi, S. 1981, *Ap&SS*, 78, 273
- Tomisaka, K., & Ikeuchi, S. 1986, *PASJ*, 38, 697
- Tomisaka, K. 1998, *MNRAS*, 298, 797
- Vallée, J. P., & Bignell, R. C. 1983, *ApJ*, 272, 131
- Vallée, J. P. 1993, *ApJ*, 419, 670
- Van Leer, B. 1977, *Journal of Computational Physics*, 23, 276
- Veilleux, S., Cecil, G., & Bland-Hawthorn, J. 2005, *ARA&A*, 43, 769
- Vernaleo, J. C., & Reynolds, C. S. 2006, *ApJ*, 645, 83
- Weaver, R., McCray, R., Castor, J., Shapiro, P., & Moore, R. 1977, *ApJ*, 218, 377
- West, J. L., English, J., Normandeau, M., & Landecker, T. L. 2007, *ApJ*, 656, 914
- Westerhout, G. 1958, *BAN*, 14, 215